

VHE gamma-ray detection of FSRQ QSO B1420+326 and modeling of its enhanced broadband state in 2020

V. A. Acciari¹, S. Ansoldi², L. A. Antonelli³, A. Arbet Engels⁴, M. Artero⁵, K. Asano⁶, D. Baack⁷, A. Babić⁸, A. Baquero⁹, U. Barres de Almeida¹⁰, J. A. Barrio⁹, J. Becerra González¹, W. Bednarek¹¹, L. Bellizzi¹², E. Bernardini¹³, M. Bernardos¹⁴, A. Berti¹⁵, J. Besenrieder¹⁶, W. Bhattacharyya¹³, C. Bigongiari³, A. Biland⁴, O. Blanch⁵, G. Bonnoli¹², Ž. Bošnjak⁸, G. Busetto¹⁴, R. Carosi¹⁷, G. Ceribella¹⁶, M. Cerruti¹⁸, Y. Chai¹⁶, A. Chilingarian¹⁹, S. Cikota⁸, S. M. Colak⁵, E. Colombo¹, J. L. Contreras⁹, J. Cortina²⁰, S. Covino³, G. D'Amico¹⁶, V. D'Elia³, P. Da Vela^{17,37}, F. Dazzi³, A. De Angelis¹⁴, B. De Lotto², M. Delfino^{5,38}, J. Delgado^{5,38}, C. Delgado Mendez²⁰, D. Depaoli¹⁵, F. Di Pierro¹⁵, L. Di Venere²¹, E. Do Souto Espiñeira⁵, D. Dominis Prester²², A. Donini², D. Dorner²³, M. Doro¹⁴, D. Elsaesser⁷, V. Fallah Ramazani²⁴, A. Fattorini⁷, G. Ferrara³, L. Foffano¹⁴, M. V. Fonseca⁹, L. Font²⁵, C. Fruck¹⁶, S. Fukami⁶, R. J. García López¹, M. Garczarczyk¹³, S. Gasparyan²⁶, M. Gaug²⁵, N. Giglietto²¹, F. Giordano²¹, P. Gliwny¹¹, N. Godinović²⁷, J. G. Green³, D. Green¹⁶, D. Hadasch⁶, A. Hahn¹⁶, L. Heckmann¹⁶, J. Herrera¹, J. Hoang⁹, D. Hrupec²⁸, M. Hütten¹⁶, T. Inada⁶, S. Inoue⁶, K. Ishio¹⁶, Y. Iwamura⁶, J. Jormanainen²⁴, L. Jouvin⁵, Y. Kajiwara²⁹, M. Karjalainen¹, D. Kerszberg⁵, Y. Kobayashi⁶, H. Kubo²⁹, J. Kushida³⁰, A. Lamastra³, D. Lelas²⁷, F. Leone³, E. Lindfors²⁴, S. Lombardi³, F. Longo^{2,39}, R. López-Coto¹⁴, M. López-Moya⁹, A. López-Oramas¹, S. Loporchio²¹, B. Machado de Oliveira Fraga¹⁰, C. Maggio²⁵, P. Majumdar³¹, M. Makariev³², M. Mallamaci¹⁴, G. Maneva³², M. Manganaro²², K. Mannheim²³, L. Maraschi³, M. Mariotti¹⁴, M. Martínez⁵, D. Mazin^{6,40}, S. Mender⁷, S. Mićanović²², D. Miceli², T. Miener⁹, M. Minev³², J. M. Miranda¹², R. Mirzoyan¹⁶, E. Molina¹⁸, A. Moralejo⁵, D. Morcuende⁹, V. Moreno²⁵, E. Moretti⁵, V. Neustroev³³, C. Nigro⁵, K. Nilsson²⁴, D. Ninci⁵, K. Nishijima³⁰, K. Noda⁶, S. Nozaki^{29*}, Y. Ohtani⁶, T. Oka²⁹, J. Otero-Santos¹, S. Paiano³, M. Palatiello², D. Paneque¹⁶, R. Paoletti¹², J. M. Paredes¹⁸, L. Pavletić²², P. Peñil⁹, C. Perennes¹⁴, M. Persic^{2,41}, P. G. Prada Moroni¹⁷, E. Prandini¹⁴, C. Priyadarshi⁵, I. Puljak²⁷, W. Rhode⁷, M. Ribó¹⁸, J. Rico⁵, C. Righi³, A. Rugliancich¹⁷, L. Saha⁹, N. Sahakyan²⁶, T. Saito⁶, S. Sakurai⁶, K. Satalecka¹³, F. G. Saturni³, B. Schleicher²³, K. Schmidt⁷, T. Schweizer¹⁶, J. Sitarek¹⁶, I. Šnidarić³⁴, D. Sobczynska¹¹, A. Spolon¹⁴, A. Stamerra³, D. Strom¹⁶, M. Strzys⁶, Y. Suda¹⁶, T. Suric³⁴, M. Takahashi⁶, F. Tavecchio³, P. Temnikov³², T. Terzić²², M. Teshima^{16,42}, N. Torres-Albà¹⁸, L. Tosti³⁵, S. Truzzi¹², A. Tutone³, J. van Scherpenberg¹⁶, G. Vanzo¹, M. Vazquez Acosta¹, S. Ventura¹², V. Verguilov³², C. F. Vigorito¹⁵, V. Vitale³⁶, I. Vovk⁶, M. Will¹⁶, and D. Zarić²⁷
R. Angioni^{43,44*}, F. D'Ammando^{45*}, S. Ciprini^{43,46}, C. C. Cheung⁴⁷, M. Orienti⁴⁵, L. Pacciani⁴⁸, P. Prajapati⁴⁹, P. Kumar⁴⁹, S. Ganesh⁴⁹, M. Minev^{50,51}, A. Kurtenkov⁵⁰, A. Marchini⁵², L. Carrasco⁵³, G. Escobedo⁵³, A. Porras⁵³, E. Recillas⁵³, A. Lähteenmäki^{54,55}, M. Tornikoski⁵⁴, M. Berton^{54,56}, J. Tammi⁵⁴, R. J. C. Vera^{54,55}, S. G. Jorstad^{57,58}, A. P. Marscher⁵⁷, Z. R. Weaver⁵⁷, M. Hart⁵⁷, M. K. Hallum⁵⁷, V. M. Larionov^{58,59,†}, G. A. Borman⁶⁰, T. S. Grishina⁵⁸, E. N. Kopatskaya⁵⁸, E. G. Larionova⁵⁸, A. A. Nikiforova^{58,59}, D. A. Morozova⁵⁸, S. S. Savchenko⁵⁸, Yu. V. Troitskaya⁵⁸, I. S. Troitsky⁵⁸, A. A. Vasilyev⁵⁸, M. Hodges⁶¹, T. Hovatta^{56,54}, S. Kiehlmann^{62,63}, W. Max-Moerbeck⁶⁴, A. C. S. Readhead⁶¹, R. Reeves⁶⁵, T. J. Pearson⁶¹

(Affiliations can be found after the references)

Received ; accepted

ABSTRACT

Context. QSO B1420+326 is a blazar classified as a Flat Spectrum Radio Quasar (FSRQ). In the beginning of 2020 it underwent an enhanced flux state. An extensive multiwavelength campaign allowed us to trace the evolution of the flare.

Aims. We search for VHE gamma-ray emission from QSO B1420+326 during this flaring state. We aim to characterize and model the broadband emission of the source over different phases of the flare.

Methods. The source was observed with a number of instruments in radio, near infrared, optical (including polarimetry and spectroscopy), ultraviolet, X-ray and gamma-ray bands. We use dedicated optical spectroscopy results to estimate the accretion disk and the dust torus luminosity. We perform spectral energy distribution modeling in the framework of combined Synchrotron-Self-Compton and External Compton scenario in which the electron energy distribution is partially determined from acceleration and cooling processes.

Results. During the enhanced state the flux of both SED components drastically increased and the peaks were shifted to higher energies. Follow up observations with the MAGIC telescopes led to the detection of very-high-energy gamma-ray emission from this source, making it one of only a handful of FSRQs known in this energy range. Modeling allows us to constrain the evolution of the magnetic field and electron energy distribution in the emission region. The gamma-ray flare was accompanied by a rotation of the optical polarization vector during a low polarization state. Also, a new, superluminal radio knot contemporaneously appeared in the radio image of the jet. The optical spectroscopy shows a prominent FeII bump with flux evolving together with the continuum emission and a MgII line with varying equivalent width.

Key words. Gamma rays: galaxies – Galaxies: jets – Radiation mechanisms: non-thermal – quasars: individual: QSO B1420+326

1. Introduction

QSO B1420+326, also known as OQ 334, is a blazar located at redshift of 0.682 (Hewett & Wild 2010). Based on its radio spectrum it has been classified as a Flat Spectrum Radio Quasar (FSRQ; Healey et al. 2007). BL Lac objects are divided between low-, intermediate- and high- synchrotron peaked (LSP, ISP, HSP), while FSRQs are usually only LSP objects. At HE (GeV) energies FSRQs populate the majority of the extragalactic gamma-ray sky. Among the associated blazars in the *Fermi*-LAT Fourth Source Catalog (4FGL; Abdollahi et al. 2020) there are 694 FSRQs compared to 1131 BL Lac objects. In the very-high-energy (VHE, ≥ 100 GeV) range despite over 60 BL Lac objects have been detected by Imaging Atmospheric Cherenkov Telescopes (IACTs), only about 8 FSRQs are known to emit in this energy range¹. There are a few probable reasons that contribute to the difference between the number of blazars detected at HE and VHE. The peak of the gamma-ray emission in the Spectral Energy Distribution (SED) of FSRQs is usually shifted to lower energies compared to BL Lac objects (see, e.g., Ghisellini 2016). Also, some of the source may have enhanced internal absorption in the radiation field of the Broad Line Region (BLR, see, e.g., Liu & Bai 2006, but note also Costamante et al. 2018) via e^+e^- pair production process. FSRQs are considered to be more luminous sources than BL Lacs, which permits them to be detected at larger cosmological distances. However, for sources located at high redshift ($z \sim 1$), the VHE gamma-ray part of the spectrum is severely absorbed in the pair production process on Extragalactic Background Light (EBL, see, e.g., Domínguez et al. 2011), hampering the discovery potential in this energy range. Softer gamma-ray spectra resulting from both effects further make detection of FSRQs with IACTs more difficult. Finally, FSRQs are known to be extremely variable (see, e.g., Meyer et al. 2019), which is another complication in observing those sources with instruments with relatively small fields of view such as IACTs. The VHE gamma-ray flux has been seen to vary even by two orders of magnitude (see, e.g., D’Ammando et al. 2019; Zacharias et al. 2019). Emission variability has been observed down to a time scale of ~ 10 minutes (Aleksić et al. 2011). Due to the strong variability, currently the most successful approach for studying the VHE gamma-ray emission of FSRQs is a follow up of alerts of enhanced activity at lower frequencies. To date all the cases of discovery of VHE gamma-ray emission from FSRQs have occurred either during short flaring activities or longer high states. A notable counterexample is PKS 1510–089, from which persistent VHE gamma-ray emission has been observed during a low flux level at HE (Acciari et al. 2018). Since the number of known VHE FSRQs is still very small, it is important to observe those objects to look for common patterns and differences in their emission and to investigate if the same processes are responsible. Moreover, the observations need to be multiwavelength and thus contemporaneously cover the broad energy range of the spectrum, which is often difficult to achieve due to fast variability.

QSO B1420+326 is known to be strongly variable, in particular in the HE range². A few periods of HE flux enhancement

from the source have been observed by *Fermi*-LAT so far, the most recent one starting in 2019 December (Ciprini & Cheung 2020). The high state continued, and based on the HE flux enhancement, the MAGIC telescopes have performed follow up observations and discovered VHE gamma-ray emission from QSO B1420+326 in 2020 January (Mirzoyan 2020). The source is the fourth most distant VHE gamma-ray source known.

Thanks to the duration of the enhanced state we were able to alert other observatories and trace the development of the flare in a broad range of wavelengths, from radio up to VHE gamma rays (e.g., Mineev et al. 2020; D’Ammando et al. 2020; Fallah Ramazani et al. 2020). Since contemporaneously to gamma-ray flaring activity in FSRQs, often ejection of new knots in their jets have been reported (see, e.g., Aleksić et al. 2014; Lindfors 2015; Rani et al. 2018), we also organized VLBI (very-long-baseline radio interferometry) observations of the source following the high state.

In this paper we report on the broadband observations of QSO B1420+326 triggered by the 2019/2020 high state and other contemporaneous multiwavelength (MWL) data and on their interpretation. In Section 2 we describe the instruments involved in the campaign, the data taken and the analysis methods. The results of the observations are reported in Section 3. In Section 4 we model the broadband emission of the source in different phases of the high state. Results are summarized in Section 5.

We use cosmological parameters $H_0=67.4$ km/s/Mpc, $\Omega_\Lambda = 0.6847$, and $\Omega_M = 0.315$ (Planck Collaboration et al. 2020).

2. Observations and data analysis

QSO B1420+326 was observed in 2020 January/February in a broad energy range by a number of instruments that either monitor the source, or had responded to a target of opportunity (ToO) announcement for a high state of the blazar, including also publicly released results. We report on the observations performed in radio (VLBA, OVRO, Metsähovi, Badary RT32), NIR (CANICA), optical polarization and photometry (Perkins, LX-200, AZT-8+ST7), optical photometry (Siena and Rozhen Observatories, ASAS-SN monitoring, MIRO/MFOC-P, REM), optical spectroscopy (LDT), optical and UV from space satellites (*Swift*-UVOT and *XMM*-OM), X-rays (*Swift*-XRT and *XMM-Newton*), HE gamma rays (*Fermi*-LAT) and VHE gamma rays (MAGIC). To put the results in the context of earlier measurements we also use archival data retrieved via the Space Science Data Center³ from the catalogs: GB6 (Gregory et al. 1996), FIRST (White et al. 1997), NVSS (Condon et al. 1998), CLASS (Myers et al. 2003), JVSPOL (Jackson et al. 2007), WISE (Wright et al. 2010), GALEX (Bianchi et al. 2011), Planck (Ade et al. 2014), 2RXS (Boller et al. 2016), SDSS (Albaret et al. 2017). In the archival data sample we also include the lowest and the highest *Swift*-XRT states of the source (MJD 57631 and 58831), and the low state observed by *Fermi*-LAT (integrated from the mission start, MJD 54683 until MJD 57754).

2.1. MAGIC

MAGIC is a system of two IACTs with a mirror dish diameter of 17 m each (Aleksić et al. 2016a). The telescopes are located in the Canary Islands, on La Palma (28.7° N, 17.9° W), at a height of 2200 m above sea level.

QSO B1420+326 has been observed by MAGIC on a few occasions following enhanced states at lower energies. We report

³ <https://www.ssd.c.asi.it/>

Send offprint requests to: contact.magic@mpp.mpg.de,

*Corresponding authors: J. Sitarek, F. D’Ammando, R. Angioni, S. Nozaki

† deceased

¹ See <http://tevcat.uchicago.edu/>, in case of some sources the classification as FSRQ or BL Lac is however uncertain.

² https://fermi.gsfc.nasa.gov/ssc/data/access/lat/msl_1c/source/OQ_334

on observations between 2019 December 31 (MJD=58848) and 2020 February 6 (MJD=58885). The observations consisted of several triggers of MAGIC Target of Opportunity program and are therefore, also due to bad weather periods, not continuous. The data selection was based on the atmospheric transmission and rates of background events. The total amount of good quality data is 14.0 hr, out of which 2.9 hr, taken between 2019 December 31 (MJD=58848) and 2020 January 4 (MJD=58852), has been taken with a special low-energy analogue trigger: SUM-Trigger-II (García et al. 2014). The data are analyzed using MARS, the standard analysis package of MAGIC (Zanin et al. 2013; Aleksić et al. 2016b). The data selection is based mainly on the atmospheric transmission measured with LIDAR (Fruck & Gaug 2015) and on hadronic background rates. The effect of atmospheric absorption is corrected using LIDAR information. The Sum-Trigger-II part of the dataset is analyzed with dedicated low-energy analysis procedures including a special image cleaning (the so-called MaTaJu cleaning) with the cleaning thresholds tuned to the extragalactic field of view of QSO B1420+326 (Shayduk 2013; Ceribella et al. 2019). For the part of the dataset during which no signal is detected, upper limits on the flux are computed following Rolke et al. (2005) at 95% confidence level.

2.2. Fermi-LAT

The Large Area Telescope (LAT) is a pair-conversion telescope, launched on 2008 June 11 (MJD=54628) as one of the two scientific instruments on board the *Fermi Gamma-ray Space Telescope* (Atwood et al. 2009). Its energy range extends down to ~ 30 MeV and up to ~ 300 GeV, with peak sensitivity at ~ 1 GeV. In the 4FGL (Abdollahi et al. 2020), QSO B1420+326 is associated to the gamma-ray source 4FGL J1422.3+3223, which has a > 100 MeV flux of $(9.1 \pm 1.3) \times 10^{-9} \text{ cm}^{-2} \text{ s}^{-1}$ and a power-law spectrum with photon index 2.38 ± 0.07 , obtained from data between 2008 June 11 (MJD=54682.65) and 2016 August 2 (MJD=57602.24). QSO B1420+326 does not appear in any of the *Fermi*-LAT hard-spectrum source catalogs (see, e.g., the 3FHL catalog, Ajello et al. 2017), which is consistent with its relatively steep spectrum.

We use the Python package *Fermipy* (Wood et al. 2017) to analyze the *Fermi*-LAT data. We use Pass8 event data (Atwood et al. 2013) and select photons of the SOURCE class, in a square region of interest (ROI) of $10^\circ \times 10^\circ$, centered at the position of the target source. We perform a binned analysis with 10 bins per decade in energy and 0.1° binning in RA and Dec, in the energy range 0.1–300 GeV, adopting the instrument response functions P8R3_SOURCE_V2. A correction for energy dispersion is included for all sources in the model except for the isotropic diffuse components. We apply a cut to include only the gamma-rays with zenith angle $< 90^\circ$ to limit contamination from the Earth's limb. We include in the model of the region all sources listed in the 4FGL within 15° from the ROI center, along with the Galactic (Acero et al. 2016) and isotropic diffuse emission models (g11_iem_v06.fits and iso_P8R3_SOURCE_V2_v1.txt, respectively).

We first perform a likelihood fit using the full *Fermi*-LAT data set available at the time of the analysis, including events in the time range 2008 August 4 to 2020 February 11 (MJD 54682.66–58890.00). We fit the full spectrum of the target source, the diffuse models, and the normalization of catalog sources within 5° as free parameters. We also optimize the target source localization, taking advantage of the ~ 3.5 extra years of data with respect to 4FGL. The detection significance is estimated with the Test Statistic (TS, Mattox et al. 1996). We search

for new sources by performing a TS map of the ROI. No significant (TS>25) new gamma-ray source is found in this analysis. Although mild excesses with TS ~ 10 are seen in the residuals, such fluctuations are to be expected when periods over long time ranges such as this are considered, and therefore we choose not to add these excesses as point sources in the ROI model. The model resulting from this initial fit is used as an input for the computation of the HE gamma-ray light curves.

The light curves are calculated by performing a likelihood fit in each time bin. The fitting strategy is designed to adjust the number of free parameters to the photon statistics available in each bin. In the *Fermi*-LAT source catalogs, a source is considered detected if TS is at least 25. In each light curve bin, we fit the full spectrum of the target source and the normalizations of the sources within 3° from the ROI center. If the target source has TS < 25 , we progressively restrict the free parameters in the fit, reloading the average model at each step. First, we reduce the sources with free normalization to a radius of 1° , then we freeze all sources except the target, and finally, if the target is not significantly detected, we only fit its normalization, leaving the spectral parameters fixed to the average value from the initial model. We consider the target source to be detected in a given time bin if TS > 9 , and the signal-to-noise ratio (that is, flux divided by its error, or $F/\Delta F$) in that bin is larger than two. If this is not the case, we reported a 95% confidence upper limit on the flux.

We report light curves with fixed binning of one day and 30 days, and one with adaptive binning (Lott et al. 2012), setting a constant relative flux uncertainty of 15%. The latter method provides an estimate of the shortest time scale over which it is possible to obtain a statistically significant detection and a robust determination of the target's spectral parameters.

We calculate 0.1–300 GeV spectral energy distributions (SEDs) in the time intervals listed in Section 3, by performing a likelihood fit in several energy bins. The number of bins is optimized as a trade-off between energy resolution and photon statistics. We also perform an analysis including data from 2008 August 4 (MJD=54682) to 2017 January 1 (MJD=57754), to compute a quiescent-state *Fermi*-LAT SED to which the high-state ones could be compared. This time range was chosen based on the monthly light curve, which shows some early signs of flaring activity between the second half of 2017 and the first half of 2018 (see Appendix A.3). This time range is quite similar to the one corresponding to the 4FGL catalog, but provides a small increase in photon statistics due to the later end time.

Finally, we calculate the probability for each single gamma ray recorded by the *Fermi*-LAT of being associated with QSO B1420+326, using the gt_srcprob tool, in order to investigate the highest energy photons in the 0.1–300 GeV energy range.

2.3. X-ray

The *Neil Gehrels Swift Observatory* (Gehrels et al. 2004) carried out 26 observations of the source between 2018 January 20 (MJD=58138) and 2020 February 10 (MJD=58889), in particular on 14 individual days between 2020 January 2 and February 10 (MJD=58850 – 58889). The pointed observations were performed with both the X-ray Telescope (XRT; Burrows et al. 2005, 0.2–10.0 keV) and the Ultraviolet/Optical Telescope (UVOT; Roming et al. 2005, 170–600nm). The hard X-ray flux of this source is below the sensitivity of the BAT instrument for the short exposures of these observations; therefore, the data from this instrument are not used. Moreover, the source is not present in the *Swift* BAT 105-month catalog (Oh et al. 2018).

All XRT observations were performed in photon counting (PC) mode. The XRT spectra are generated with the *Swift* XRT data products generator tool at the UK Swift Science Data Centre⁴ (for details see Evans et al. 2009). Ancillary response files are generated with `xrtmkarf`, and account for different extraction regions, vignetting and point-spread function corrections. We use the spectral redistribution matrices `v014` in the Calibration data base maintained by HEASARC. Some of the spectra have very few photons, and so we are not able to use χ^2 statistics. To maintain the homogeneity in our analysis, we grouped the obtained spectra using the task `grppha` to have at least one count per bin and we perform the fit with the Cash statistics (Cash 1979). The data collected during 2019 June 27 and 29 (MJD=58661 and 58663) are summed in order to have enough statistics to obtain a good spectral fit. We fit the spectra with an absorbed power-law using the photoelectric absorption model `tbabs` (Wilms et al. 2000), with a neutral hydrogen column density fixed to its Galactic value ($1.08 \times 10^{20} \text{ cm}^{-2}$; Ben Bekhti et al. 2016). We apply also a log-parabola model to the XRT data, testing if this model is preferred over a single power-law model on a statistical basis by applying an F-test. The log-parabola model is preferred over a simple power-law model only on 2020 January 28 and at 95% confidence level. However, this can be due to the low statistics of the single XRT observations.

XMM-Newton (Jansen et al. 2001) observed the source on 2020 January 24 between 04:44:07 and 11:49:07 (MJD 58872.3 – 58872.5) for a total duration of 25 ks (observation ID 0850180201). The 3 EPIC cameras were operated in the large-window mode with medium filter. The data are reduced using the *XMM-Newton* Science Analysis System (SAS v16.0.0), applying standard event selection and filtering. Inspection of the background light curves show that no strong flares were present during the observation, with good exposure times of 20, 24 and 24 ks for the pn, MOS1 and MOS2, respectively. For each of the detectors the source spectrum is extracted from a circular region of radius 30 arcsec centered on the source, and the background spectrum from a nearby region of radius 30 arcsec on the same chip. All the spectra are binned to contain at least 20 counts per bin to allow for χ^2 -based spectral fitting. All spectral fits are performed over the 0.3–10 keV energy range using XSPEC v.12.10.1. The energies of spectral features are quoted in the source rest frame. All errors are given at the 90% confidence level. The data from the three EPIC cameras are initially fitted separately, but since good agreement is found (< 5%) we proceed to fit them together. Galactic absorption is included in all fits using the `tbabs` model.

Three different models are applied: a simple power-law, a broken power-law, and a log-parabola model. The results of the fits are presented in Table 1. The F-test shows an improvement of the fit using both a broken power-law and a log-parabola model with respect to the simple power-law, with the log-parabola model providing the best fit.

In order to check for the presence of intrinsic absorption, a neutral absorber at the redshift of the source is added to this model, but it does not improve the fit quality and thus is not required. Moreover, no Fe line was detected in the spectrum. The 90% upper limit on the equivalent width (EW) of a narrow emission line at 6.4 keV is $\text{EW} < 10 \text{ eV}$.

Model	Parameter	Value
Power-law	Γ	1.95 ± 0.01
	Flux (0.3–10 keV)	$(5.2 \pm 0.1) \times 10^{-12}$
	$\chi^2/\text{d.o.f.}$	1627.79/379
Broken Power-law	Γ_1	2.38 ± 0.05
	E_{break}	$1.22^{+0.10}_{-0.08}$
	Γ_2	1.58 ± 0.04
	Flux (0.3–10 keV)	$(6.0 \pm 0.1) \times 10^{-12}$
	$\chi^2/\text{d.o.f.}$	472.21/377
Log Parabola	α	2.12 ± 0.01
	β	-0.60 ± 0.03
	Flux (0.3–10 keV)	$(6.2 \pm 0.1) \times 10^{-12}$
	$\chi^2/\text{d.o.f.}$	432.42/378

Table 1. Summary of fits to the 0.3–10 keV *XMM-Newton* spectrum of the source. Fits also include absorption fixed at the Galactic value. Flux and E_{break} (in the source rest frame) are given in units of $\text{erg cm}^{-2} \text{ s}^{-1}$ and keV, respectively.

2.4. Optical and UV from space-based telescopes

During the *Swift* pointings, the UVOT instrument observed QSO B1420+326 in all its optical (*v*, *b* and *u*) and UV (*w1*, *m2* and *w2*) photometric bands (Poole et al. 2008; Breeveld et al. 2010). For each epoch, possible multiple exposures in the same filter are first summed with the task `uvot.imsum` and then analyzed using the `uvot.source` task included in the HEASOFT package (v6.28) with the 20201026 release of the Swift/UVOTA CALDB. We check if the observations are affected by small-scale sensitivity problems⁵. Source counts are extracted from a circular region of 5 arcsec radius centered on the source, while background counts are derived from a circular region of 20 arcsec radius in a nearby source-free region.

The Optical Monitor (OM) on board of the *XMM-Newton* satellite observed the source in the *u*, *w1*, *m2*, and *w2* filters in imaging mode together with a fast readout window. The total exposure times of the imaging observations are: 3500 s (*u*), 3500 s (*w1*), 4400 s (*m2*) and 4400 s (*w2*). The data are processed using the SAS tasks `omichain` and `omfchain`.

The UVOT and OM flux densities are corrected for extinction using the $E(B-V)$ value of 0.010 from Schlafly & Finkbeiner (2011) and the extinction laws from Cardelli et al. (1989).

2.5. Optical from ground-based telescopes

The REM telescope (Zerbi et al. 2001; Covino et al. 2004), a robotic telescope located at the ESO Cerro La Silla observatory (Chile), performed optical photometric observations of QSO B1420+326 in the period 2020 January 24–February 6 (MJD=58872 – 58885). Observations were carried out with the Optical Slitless Spectrograph (ROSS2) obtaining three 240 s integration images in the optical *g'*, *r'*, *i'* bands. The REM data presented here were obtained as ToO observations triggered by the high gamma-ray flux observed by *Fermi*-LAT after the MAGIC detection. Instrumental magnitudes are obtained via aperture photometry and absolute calibration is performed by means of secondary standard stars in the field reported by the AAVSO Photometric All-Sky Survey (APASS) catalog⁶. Transformation

⁵ https://swift.gsfc.nasa.gov/analysis/uvot_digest/sss_check.html

⁶ <https://www.aavso.org/apass>

⁴ http://www.swift.ac.uk/user_objects

between the $u'g'r'i'z'$ and UBVR photometric systems are performed using the equations reported in Jester et al. (2005)⁷.

Optical photometric (BVRI) and polarimetric (R band) observations were carried out at the 1.83 m Perkins telescope (Flagstaff, AZ, USA), 40 cm LX-200 telescope (St.Petersburg, Russia) and 70 cm AZT-8 telescope (Crimea) from 2020 January 23 to April 21 (MJD 58871 – 58960). The photometric data are reduced using differential aperture photometry with respect to comparison stars in the quasar field⁸. The polarimetric observations obtained at the Perkins telescope were performed and reduced in the same manner as described in Jorstad et al. (2010). The details of polarimetric observations carried out at the LX-200 and AZT-8 telescopes can be found in Larionov et al. (2008).

Photometric optical observations of QSO B1420+326 were carried out with the MFOSC-P instrument (Srivastava et al. 2018), used in imaging mode, mounted on the 1.2 m telescope of Mount Abu IR Observatory (MIRO⁹). The source was observed in B, V, R, and I bands (Johnson-Cousins filters) on 2020 February 2 and 6 (MJD=58880 and 58885). MIRO is located at Gurushikhar peak in Mount Abu, India, at altitude of 1680 m and is operated by Physical Research Laboratory (PRL), Ahmedabad, India.

The optical data from National Astronomical Observatory (NAO) Rozhen, Bulgaria were obtained between 2020 January 24 and 26 (MJD=58872 – 58874). We used the 2-m RCC telescope with Andor iKon-L CCD camera (2048x2048 px, 13.5 $\mu\text{m}/\text{pixel}$) and the 50/70 cm Schmidt telescope with FLI PL-16803 CCD camera (4096x4096 px, 9 $\mu\text{m}/\text{pixel}$). Additional observations were carried out 2020 January 31 to February 2 (MJD=58879 - 58881) at Student Astronomical Observatory (SAO) Plana (Ovcharov et al. 2014) with 35 cm Newton telescope and SBIG STL-11000M CCD Camera (4008x2672 px, 9 $\mu\text{m}/\text{pixel}$). All cameras are equipped with standard photometric UBVR Johnson-Cousins filters.

The data are reduced (including bias subtraction, flat-fielding, and cosmic-ray correction) and analyzed using standard photometry packages from IRAF¹⁰. For each image the PSF value is measured and aperture photometry is applied. Standard stars from the SDSS DR12 and VizieR catalogs are used for photometric calibration after applying transformation equations¹¹.

The Astronomical Observatory of the University of Siena observed QSO B1420+326 in its program devoted to optical photometry of blazars in support of MAGIC. The observatory runs a remotely operated 30 cm Maksutov-Cassegrain telescope installed on a Comec 10micron GM2000-QCI equatorial mount. The focal plane hosts a Sbig STL-6303 camera equipped with a 3072 x 2048 pixels KAF-6303E sensor; Johnson-Cousins BVRI filters are available. Multiple 300 s images of QSO B1420+326 were acquired at each visit. After standard dark current subtraction and flat-fielding, images are averaged and aperture photometry is performed on the average frame by means of the MaximDL software package. Reference and check stars in the field of view are selected from the APASS9 (Henden, et al. 2016) catalog. The reference R magnitudes are derived from those reported in the same APASS9 catalog after conversion between the two

different photometric systems, following a formula taken from Munari (2012).

Additionally we use publicly available data in V-band and g-band of ASAS-SN (Shappee et al. 2014; Kochanek et al. 2017).

Conversion of magnitudes to energy fluxes is done using zero points of Bessell et al. (1998). Correction for the Galactic extinction is applied using the $E(B-V)$ value of 0.011 from Schlafly & Finkbeiner (2011) and the extinction laws from Cardelli et al. (1989).

We have performed observations of optical spectra of the quasar QSO B1420+326 using the 4.3 m Lowell Discovery Telescope (LDT; Lowell Obs., Flagstaff, AZ) equipped with the DeVeney spectrograph and the Large Monolithic Imager (LMI), in response to the detection of the source at VHE by MAGIC on 2020 January 21 (MJD=58869). We employed a grating setting of 300 grooves per millimeter, which provides spectra from 3300Å to 7500Å with a dispersion of 2.17 Å per pixel, a blaze wavelength of 5000Å and a slit width of 2.5''. The spectroscopic observations were performed on 2020 January 28 (MJD 58876.578), February 8 (MJD 58887.497) and 25 (MJD 58904.368). During this month the brightness of the quasar fell from 14.6 mag to 16.25 mag in R band. Each observation of the quasar consisted of 3 exposures of 600 s (900 s on February 25). Observations of a comparison star HD126944 of A type, located $\sim 86'$ from the quasar, were performed before and after target observations, with two 30 s exposures for each observation. Bias and flat-field images were obtained regularly. The LDT allows a switch between different instruments in 2-3 min. Therefore, photometry of the quasar using the LMI in V and R filters were performed just before or after spectral observations to calibrate the spectra. The observations are reduced using programs written in IDL (v.8.6.1) that implement the technique described in Vacca et al. (2002) developed for reduction of spectra obtained with SpeX at the NASA Infrared Telescope Facility on Mauna Kea.

2.6. NIR

The NIR observations were carried out with the camera CANICA (Carrasco et al. 2017), along with the Guillermo Haro 2.1m telescope (OAGH), located at Cananea Sonora Mexico. The camera is based on a Hawaii detector of 1024 by 1024 pixels with a plate scale of 0.32 arcsec per pixel. The data are part of the monitoring program "NIR photometry of AGNs with Gamma Ray emission detected by *Fermi*-LAT". Relative photometry is obtained with respect to the 2MASS point sources included in the field of view (5.5 arcmin). Absolute fluxes are obtained adopting the zero point values of 2MASS derived by Cohen et al. (2003). The host galaxy is not detected in IR by the 2MASS survey in any of the three bands, resulting in an upper limit of $H \sim 17.7$ mag, much weaker than 13–11 mag observed by CANICA during the investigated period. Therefore the effect of the host galaxy is negligible.

2.7. Radio

The 37 GHz observations were made with the 13.7 m diameter Metsähovi radio telescope. The detection limit of the telescope at 37 GHz is on the order of 0.2 Jy under optimal conditions. Data points with a signal-to-noise ratio < 4 are handled as non-detections. The flux density scale is set by observations of DR 21. Sources NGC 7027, 3C 274 and 3C 84 are used as secondary calibrators. A detailed description of the data reduc-

⁷ <https://www.sdss.org/dr16/algorithms/sdssUBVRITransform/>

⁸ see https://vo.astro.spbu.ru/vlar/opt_thumbs/b21420_1.png

⁹ <https://www.prl.res.in/~miro/>

¹⁰ <http://iraf.noao.edu/>

¹¹ <http://www.sdss3.org/dr8/algorithms/sdssUBVRITransform.php#Lupton2005>

Period	MJD	comment
A	58846.5 - 58853.5	pre-flare
B	58867 - 58868	optical flare
C	58868.3 - 58870.3	VHE flare
D	58873.5 - 58880.5	post-flare

Table 2. Periods selected for the SED modeling (the colors of the period tag correspond to colors used in the figures)

tion and analysis is given in Teräsraanta et al. (1998). The error estimate in the flux density includes the contribution from the measurement rms and the uncertainty of the absolute calibration.

We also use publicly available 15 GHz OVRO data (Richards et al. 2011) and 8.63 GHz data from Badary RT32 reported in (Kharinov 2020).

We requested Director’s Discretionary Time (DDT) with the Very Long Baseline Array (VLBA) following the gamma-ray activity and VHE detection of the quasar QSO B1420+326 and were granted 6 epochs of observations of the source separated by approximately 1 month intervals (ID BD227), with 8 hrs per epoch. Thus far, we have obtained 3 epochs of observations under the project, on 2020 March 8, May 10, and June 6 (MJD=58916, 58979, 59006). The observations were performed with all 10 antennas in continuum, dual circular polarization mode at 43 GHz using 4 intermediate frequency bands (IFs), each of 64 MHz width. The data were correlated at the National Radio Astronomy Observatory (NRAO, Socorro, NM) using the VLBA DiFX software correlator. Five sources were observed at each epoch (QSO B1420+326 3C 279, 3C 345, PKS 1055+18, and B2 1308+326), with 60% of the time devoted to the main target, QSO B1420+326. The sources 3C 279, 3C 345, and PKS 1055+018 are used for fringe finding during the correlation. The data are reduced using the Astronomical Image Processing System software (AIPS, van Moorsel, Kembal, & Greisen 1996) and Difmap package (Shepherd 1997) in the same manner as described in Jorstad et al. (2017), except without averaging of the final calibrated data over IFs. We use the sources observed along with QSO B1420+326 to perform absolute calibration of the electric vector position angle (EVPA), since these sources are monitored in the VLBA-BU-BLAZAR program¹², so that their polarization properties at 43 GHz are known.

3. Results

In Fig. 1 we present the MWL light curve summarizing the evolution of the flare. Based on the VHE state of the source we define three periods selected for the further spectral analysis: A: 2019 December 29 to 2020 January 5 (MJD=58846.5 – 58853.5): without VHE gamma-ray detection, C: 2020 January 20 to 22 (MJD=58868.3 – 58870.3): VHE gamma-ray flare, D: 2020 January 25 to February 1 (MJD=58873.5 - 58880.5): detection over longer time scale. In addition we define the fourth period: B: 2020 January 19 to 20 (MJD=58867 – 58868), which does not have simultaneous MAGIC data, but contains the peak of the optical and IR flare as well as one of the local peaks of HE emission. The four periods (referred to throughout the paper as periods A-D) are summarized in Table 2. In each period we construct a broadband SED (see Fig 2).

In the case of gamma-ray data all observations performed within a given time window are summed. X-ray data available from different observations are stacked for the period D, while in the other periods a single *Swift*-XRT observation is available and

used. On the other hand, the low-energy data (radio up to UV) have mostly lower uncertainties and hence are more sensitive to variability. Therefore, if more than one measurement was taken at a given time period we average all the measurements and take the standard deviation of the measurements as the measure of its uncertainty. A similar approach for constructing a broadband SED has been applied, e.g., in Acciari et al. (2018).

3.1. VHE gamma-ray emission

The first detection of the VHE gamma-ray emission from QSO B1420+326 was achieved on 2020 January 20 (MJD=58868). A highly significant detection of 14.3σ is obtained in 1.6 hr of effective time (see Fig. 3). In the subsequent period of 2020 January 26 to February 1 (MJD=58874 – 58880) further hints of signal are obtained, with the highest significance of the excess (6.6σ) on the night of 2020 January 31 (MJD=58879), which has also the longest exposure of 2.5 hr.

During the flare (period C), the flux observed by MAGIC above 100 GeV reached $(7.8 \pm 1.3_{\text{stat}}) \times 10^{-11} \text{cm}^{-2} \text{s}^{-1}$. The observed spectrum in this period can be described by a power-law: $dN/dE = (2.49 \pm 0.31_{\text{stat}}) \times 10^{-9} (E/100 \text{ GeV})^{-4.22 \pm 0.24_{\text{stat}}} [\text{TeV}^{-1} \text{cm}^{-2} \text{s}^{-1}]$. Correcting for the EBL absorption according to Domínguez et al. (2011), the unattenuated spectrum can be described as $dN/dE e^{\tau_{\text{EBL}}(E)} = (4.04 \pm 0.54_{\text{stat}}) \times 10^{-9} (E/100 \text{ GeV})^{-3.57 \pm 0.29_{\text{stat}}} [\text{TeV}^{-1} \text{cm}^{-2} \text{s}^{-1}]$.

After the flare (period D), significant gamma-ray emission is detected again with 5.6σ , but at about half the flare level: $F_D(> 100 \text{ GeV}) = (3.9 \pm 0.6_{\text{stat}}) \times 10^{-11} \text{cm}^{-2} \text{s}^{-1}$. The observed spectrum in this period can be described: $dN/dE = (0.91 \pm 0.13_{\text{stat}}) \times 10^{-9} (E/100 \text{ GeV})^{-3.90 \pm 0.25_{\text{stat}}} [\text{TeV}^{-1} \text{cm}^{-2} \text{s}^{-1}]$. Correcting for the EBL absorption according to Domínguez et al. (2011), the spectrum can be described as $dN/dE e^{\tau_{\text{EBL}}(E)} = (1.64 \pm 0.22_{\text{stat}}) \times 10^{-9} (E/100 \text{ GeV})^{-2.87 \pm 0.36_{\text{stat}}} [\text{TeV}^{-1} \text{cm}^{-2} \text{s}^{-1}]$. Despite enhancement of the VHE gamma-ray flux by a factor of two, the spectral indices during and after the flare are consistent within 1.5σ . It should be noted however that, in particular in period D, the uncertainties of the photon index are large.

Before the flare (period A), possibly due to shorter observations under less favorable zenith angle, no significant emission is detected and only a 95% C.L. limit of $< 4.1 \times 10^{-11} \text{cm}^{-2} \text{s}^{-1}$ can be placed for the flux above 100 GeV. The limit is comparable to the emission detected from the source in period D. The SED of QSO B1420+326 observed by MAGIC in different periods is shown in Fig. 4.

3.2. HE gamma rays

The first detection of a HE outburst from B2 1420+326 was reported in 2018 December (Ciprini 2018), with a flux increase by more than two orders of magnitude with respect to the average 4FGL value and significant spectral hardening. A similar spectral hardening has been reported in 2019 July (Angioni 2019), where the first evidence of $> 10 \text{ GeV}$ photons was provided, and again in 2020 January (Ciprini & Cheung 2020).

The daily *Fermi*-LAT light curve is shown in Fig. 1, including the flux (second panel) and photon index (third panel). Both the flux and the photon index are significantly variable in this time interval, based on a simple χ^2 test. The *Fermi*-LAT recorded a peak daily flux ($E > 100 \text{ MeV}$) of $(2.6 \pm 0.2) \times 10^{-6} \text{cm}^{-2} \text{s}^{-1}$ on 2020 January 19 (MJD=58867), corresponding to about 300 times the average value reported in the 4FGL catalog. The highest-energy photon observed by the *Fermi*-LAT was recorded

¹² www.bu.edu/blazars/VLBAproject.html

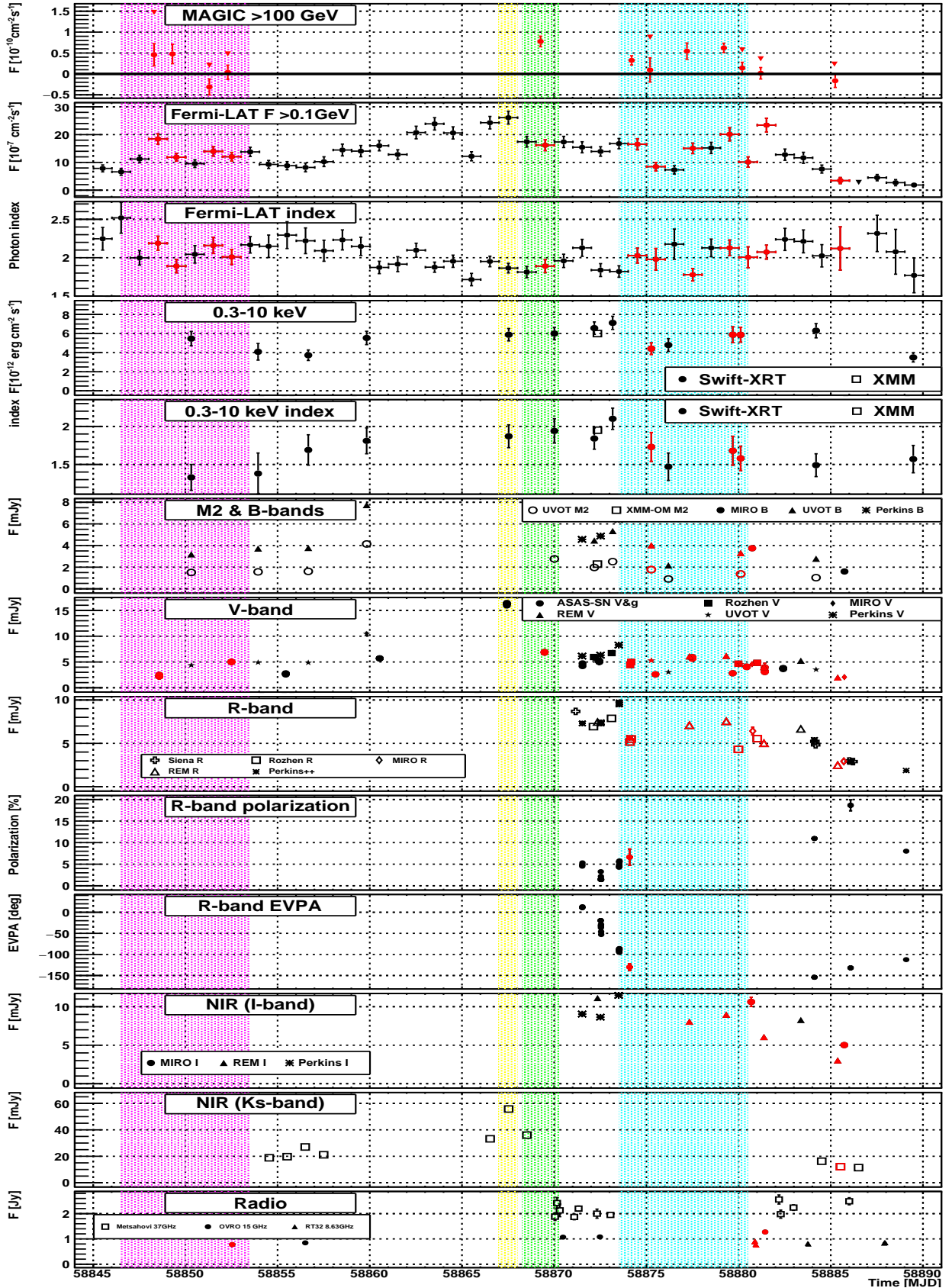


Fig. 1. MWL light curve of QSO B1420+326 between 2019 December 28 (MJD=58845) and 2020 February 11 (MJD=58890); see titles and legends of individual panels. Optical and UV observations are corrected for the Galactic attenuation. The points in red are contemporaneous (± 12 hr) with MAGIC observations. The shaded regions show the time ranges of the four considered flare evolution periods (see Table 2). Flux upper limits in the first two panels are shown with downward triangles.

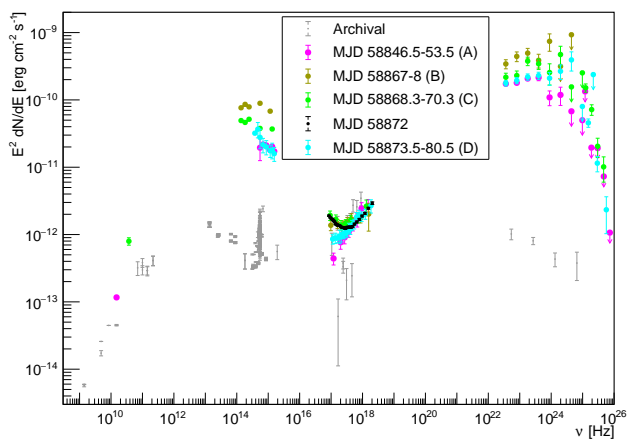


Fig. 2. MWL SED of QSO B1420+326 in 2020 January/February. Points follow the colors of the shaded regions in Fig. 1. In addition in black XMM points taken on 2020 January 24 (MJD=58872) are shown. MAGIC points are not corrected for the EBL absorption. Gray points show archival data (most from the ASI Space Science Data Center, but also including low-state *Fermi*-LAT spectrum and lowest and highest X-ray spectrum from *Swift*-XRT).

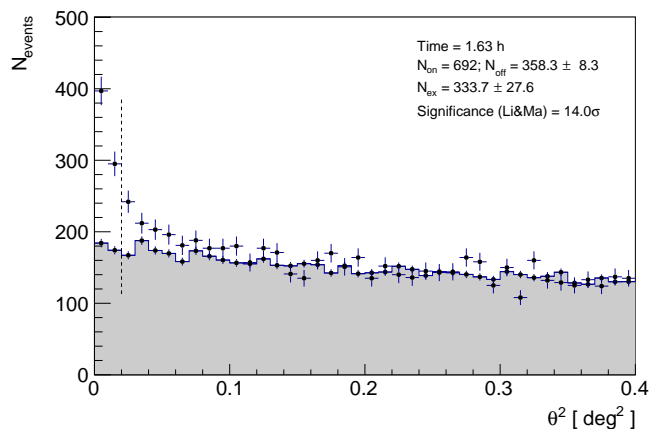


Fig. 3. Distribution of the squared angular distance between the source nominal and event reconstructed directions (points) and corresponding background estimation (shaded region) for the night of 2020 January 20 (MJD=58868) of MAGIC observations. Vertical line shows the cut value below which the event statistics are given in the inset.

two days prior (2020 January 17, MJD=58865), with an energy of ~ 150 GeV, providing the first indication of VHE emission from QSO B1420+326¹³. Accordingly, the *Fermi*-LAT recorded the hardest daily spectrum on the same date, with a photon index of 1.72 ± 0.08 , a flux of $(1.2 \pm 0.2) \times 10^{-6} \text{ cm}^{-2} \text{ s}^{-1}$ and a TS of 496. We also note that the photon index was consistently harder than the 4FGL catalog value (2.38 ± 0.07) during most of the time range shown in Fig 1.

The adaptively binned light curve is shown in Fig. 5. The shortest adaptive bin is centered on 2020 January 19, 00:17:45 (MJD=58867.012), and has a width of ~ 6 hours. The highest flux is recorded in the same bin, reaching a value of $(3.6 \pm 0.5) \times 10^{-6} \text{ cm}^{-2} \text{ s}^{-1}$, i.e. 400 times higher than the 4FGL value.

We note that a test for spectral curvature was performed in all time bins of all light curves, and a power-law spectrum was found to be the best representation in all time intervals.

¹³ The probability of this photon being associated with the target source is $> 99.9\%$, as obtained from the *gtsrcprob* tool.

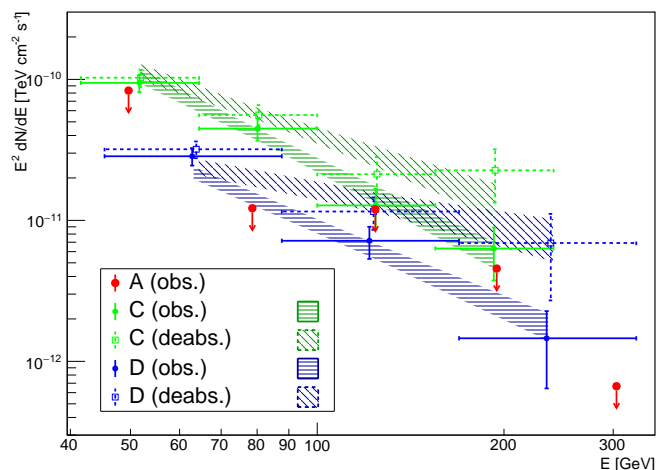


Fig. 4. SED of QSO B1420+326 observed by MAGIC in periods A, C and D (see legend): observed (filled circles) and corrected for EBL absorption (empty circles).

Additionally, we perform a likelihood fit over the full time interval included in Fig. 1, to characterize the average source properties in the HE band in this flaring state. For this time interval, the LogParabola model is preferred ($TS_{curv} = 36$ ¹⁴) with respect to a simple power law to describe the gamma-ray spectrum of the source. It yields a photon flux $(1.09 \pm 0.02) \times 10^{-6} \text{ cm}^{-2} \text{ s}^{-1}$, and spectral parameters $\alpha = 1.97 \pm 0.02$, and $\beta = 0.07 \pm 0.01$ ¹⁵. We also verify that there are no new significant point sources in addition to the initial 4FGL model during this period.

Finally, as mentioned in Section 2, we perform separate likelihood fits corresponding to the periods used to build time-resolved SEDs. The results of these fits are summarized in Table 3, together with the ones for the quiescent state.

State	Flux ^a	Photon index	TS
Quiescent	0.86 ± 0.13	2.40 ± 0.08	218
A	115 ± 6	2.04 ± 0.04	1942
B	260 ± 20	1.88 ± 0.07	688
C	160 ± 20	1.88 ± 0.06	927
D	121 ± 7	1.93 ± 0.04	2280

^a Total flux in the energy range 0.1-300 GeV in units of $10^{-8} \text{ cm}^{-2} \text{ s}^{-1}$.

Table 3. Results of *Fermi*-LAT analysis on the different activity states of QSO B1420+326. The time periods are defined in Table 2.

3.3. X-ray

There is no strong variability of the X-ray flux in the investigated period with an increasing trend from 2020 January 05

¹⁴ $TS_{curv} = 2(\ln L_{LP} - \ln L_{PL})$ is used to check if a statistically significant curvature is detected using a LogParabola model compared with the PowerLaw model, where $\ln L$ indicates the logarithm of the likelihood for each model. A source is considered to have a statistically significant curvature if $TS_{curv} > 25$.

¹⁵ The functional form of the LogParabola spectral model is $dN/dE = N_0(E/E_b)^{-(\alpha+\beta \log(E/E_b))}$, where N_0 is the normalization, E_b is the reference energy at which N_0 is measured, α is the slope and β is the curvature parameter.

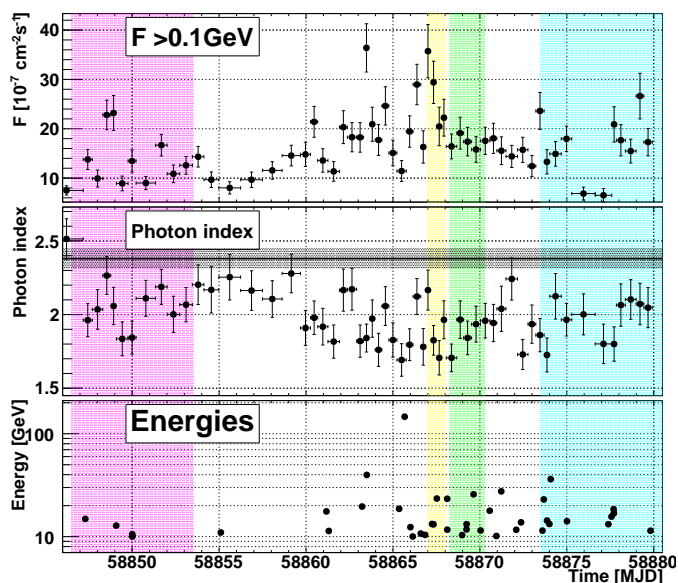


Fig. 5. *Fermi*-LAT adaptively binned light curve of QSO B1420+326 in January 2020. The vertical shaded areas follow the color coding of Fig. 1. *Top panel:* 0.1–300 GeV photon flux. *Middle panel:* power-law photon index (the horizontal shaded area represents the average value from the 4FGL with its uncertainty). *Bottom panel:* $E > 10$ GeV photons associated with QSO B1420+326 with probability $> 80\%$.

(MJD=58853) to 2020 January 25 (MJD=58873), where a peak flux a factor of 2 higher is observed. However there is a clear variability of the X-ray spectral index from hard values before the flare to much softer at the time around the optical and gamma-ray flares, back to hard values. This indicates a shift of the synchrotron peak of the source and connected with it, the shift of the crossing point between the synchrotron and the IC component. This is clearly visible in the X-ray spectra during the flare and during *XMM-Newton* observations (see Fig. 2). Results of the spectral fits to individual days of *Swift*-XRT observations are given in Appendix A.2.

3.4. Optical

Compared to the historical measurements, the optical emission is ~ 1.5 orders of magnitude higher throughout the investigated period. Moreover, during that period a strong optical flare is observed on 2020 January 19 (MJD=58867) with a variability time scale of the order of a few days. V-band observations performed during one of the *Fermi*-LAT peaks show an increase by nearly an order of magnitude with respect to observations at the beginning of Period A. Similar variability pattern is seen also in IR and UV ranges. However, the spectral shape in the IR-UV range varies during the investigated period, with the spectrum becoming bluer (harder) during the optical flare (see Fig. 2). This is consistent with the X-ray behavior of the source that also suggests a shift of the synchrotron peak position. Recently other occurrences of comparable flaring activity in the optical had been observed (e.g., in July 2019, Marchini et al. 2019), reporting a $R = 13.7$ magnitude even slightly brighter than the brightest R point in Fig 1.

Also optical polarization shows interesting behavior with a dip of the polarization percentage at a few per cent level and a concurrent rotation by $\sim 150^\circ$. Similar EVPA rotation during low level of polarization has been also seen contemporaneous with VHE emission in, e.g., PKS 1510–089 (Aleksić et al. 2014).

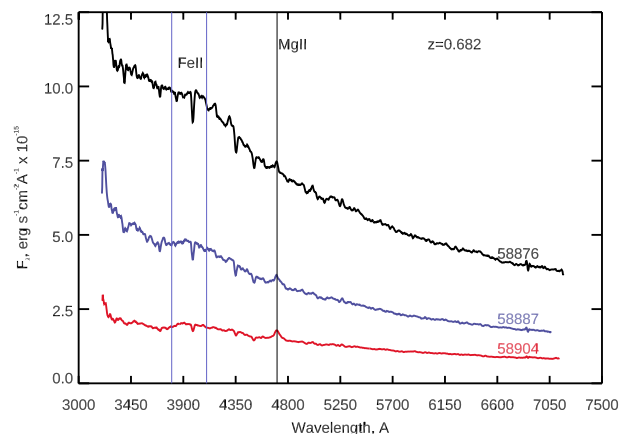


Fig. 6. Optical spectra of QSO B1420+326 obtained with the LDT; the spectra are in the observer’s frame.

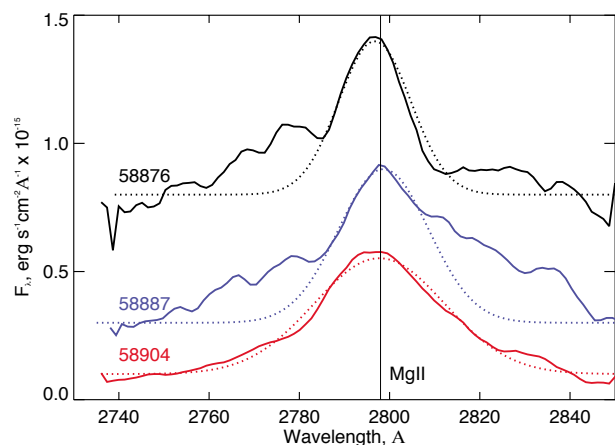


Fig. 7. Observed (solid) and modeled (dotted) MgII line of QSO B1420+326 in the rest frame at three epochs. The lines on 2020 January 28 (MJD=58876), February 8 (MJD=58887), and February 25 (MJD=58904) are shifted by values of 0.8 0.3, and 0.1, respectively, for clarity.

Large variability of EVPA (down to a time scale of 3 hours) has been also seen in PKS 0736+017, another FSRQ during the period of VHE gamma-ray detection (H. E. S. S. Collaboration et al. 2020).

3.5. Optical Spectroscopy

Fig. 6 presents the optical spectra of QSO B1420+326 obtained with LDT at three epochs of different activity states (taken mostly after the gamma-ray flaring activity). The spectra show the presence of MgII emission line at $\lambda = 4706 \text{ \AA}$ (rest wavelength of 2798 \AA) and a bump between 3800 \AA and 4100 \AA (rest frame $\sim 2260\text{--}2450 \text{ \AA}$). The latter appears to be part of an FeII emission complex, whose strongest UV lines fall in the $2200\text{--}2600 \text{ \AA}$ range (e.g., Baldwin et al. 2004). The spectra also include three prominent absorption lines at $\lambda \sim 4001 \text{ \AA}$, 4337 \AA and 4477 \AA that intensify as the quasar brightens. The absorption lines are most likely intervening MgII systems at redshifts of $z \approx 0.43, 0.55, \text{ and } 0.60$, respectively.

We analyze the characteristics of the MgII emission line and FeII bump as a function of continuum brightness. Fig. 7 shows an approximate Gaussian fit to the MgII line, while Fig. 8 plots similar modeling of the FeII bump at all three epochs. The parameters of the Gaussian and velocities of clouds, as well as the flux of the lines, are given in Table 4, although we are unable to estimate the velocity of gas producing FeII lines, since the bump consists of >100 lines. There is a significant difference between the MgII line and FeII bump behavior: i) the flux of the MgII line remains constant within 1σ uncertainty independent of the continuum brightness, while the FeII bump increases in flux with the continuum level (see Fig. 9); ii) the central wavelength of the MgII line fits does not show a shift with respect to the rest wavelength, while λ_0 of the FeII bump shifts toward the blue side as the time after the VHE event passes. Unfortunately, it is not possible to distinguish whether the shift is due to a relative change of the brightness of lines that form the FeII bump, or due to gas motion toward the observer; and iii) the FWHM of the FeII bump is very stable despite the correlation of its flux with the continuum level, while the velocity of gas where the MgII line originates increases with time after the VHE event. We note also a significant change of the equivalent width (EW) of the MgII line with the continuum, with EW decreasing as the continuum rises. This questions the identification of QSO B1420+326 as a FSRQ, however, Table 4 shows that at the lower levels of activity $EW > 5\text{\AA}$ for the MgII line¹⁶.

The increase in the flux of the FeII bump with the continuum and a possible motion of gas producing FeII lines toward the observer are quite interesting. The short time lag between the continuum and line variability suggests that the FeII emission-line region is much smaller than the region producing the MgII line and/or lies close to the line of sight. It is possible that the non-thermal jet is interacting with an FeII-emitting cloud, while the MgII emission is excited by the underlying thermal accretion disk continuum, which varies on a much longer time scale.

We adopt an approach suggested by Ghisellini et al. (2014) (see also references therein), who used an estimate of the accretion disk (AD) luminosity based on the luminosity of the BLR, $L_{AD} \approx 10 L_{BLR}$. The known flux density of the MgII line, combined with the BLR template constructed by Vanden Berk et al. (2001) for a composite emission spectrum of a quasar using SDSS spectra, allow us to estimate the total luminosity of the BLR in QSO B1420+326 $L_{BLR} = (1.8 \pm 0.2) \times 10^{45} \text{ erg s}^{-1}$. This, for luminosity distance of 4256.4 Mpc translates to $L_{AD} \approx 2 \times 10^{46} \text{ erg s}^{-1}$, with an uncertainty of a factor of ~ 2 , as suggested by Ghisellini et al. (2014). Interestingly, the obtained luminosity of the accretion disk is rather high, in the high-end part of values shown for other sources Ghisellini et al. (2014).

3.6. Radio

Moderate variability is seen in radio observations (see also Appendix A.3). OVRO data during the investigated period show a gradual increase of the flux. No monotonous behavior is seen in flux at 37 GHz by Metsähovi, but a constant fit can be rejected at $\chi^2/N_{\text{dof}} = 51/21$. The amplitude of the variability is $\sim 10\%$.

The total and polarized intensity VLBA maps of QSO B1420+326 are presented in Fig. 10. The images exhibit the bright VLBI core located at the north-western end of the jet and a weak extended jet at position angle $\sim 130^\circ$.

¹⁶ EW of 5\AA is the classical threshold between BL Lac and FSRQ objects, see, e.g., Sambruna et al. (1996)

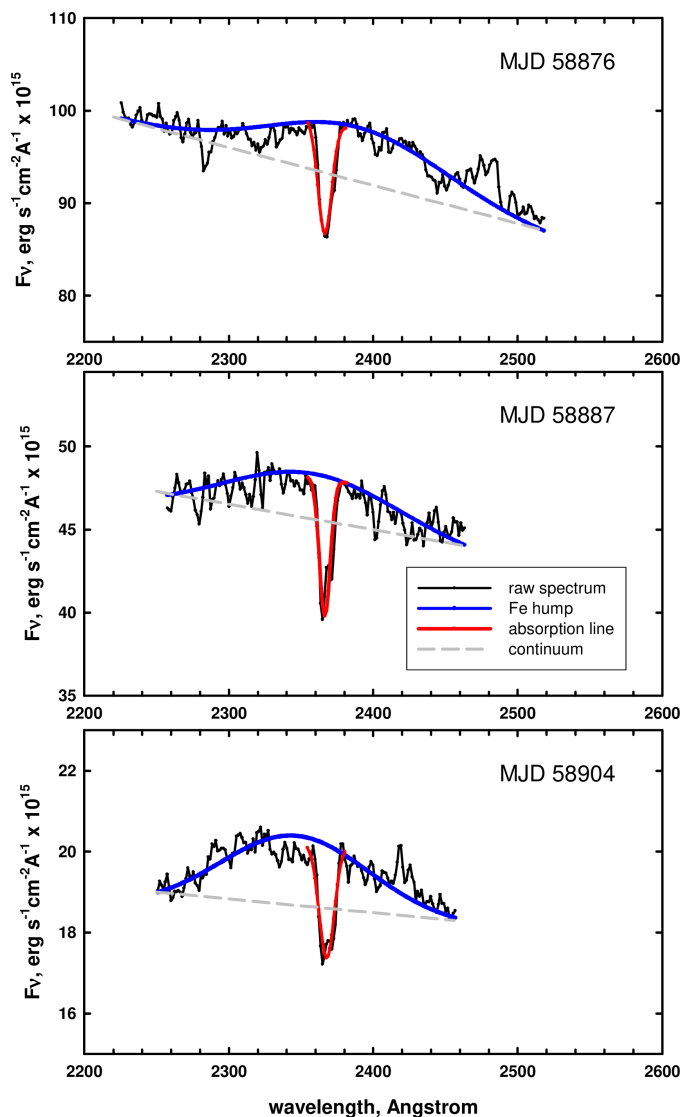


Fig. 8. Observed (black) and modeled (blue) FeII bump of QSO B1420+326 at three epochs in the rest frame; red lines represent Gaussian fits to absorption lines, and gray dashed lines indicate the continuum level.

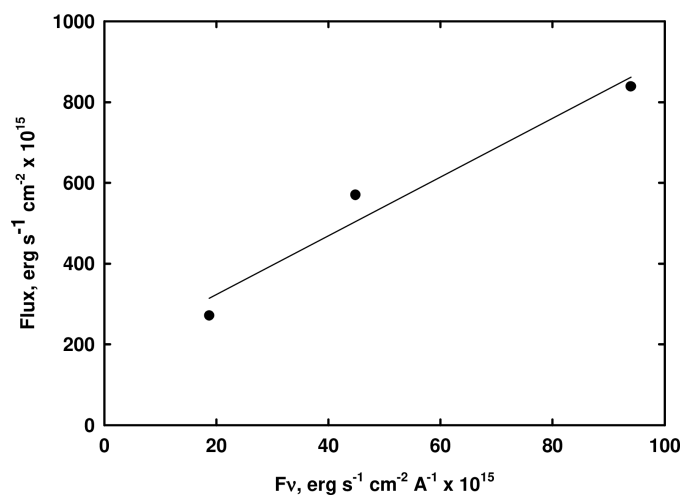


Fig. 9. Dependence between flux of the FeII bump and flux density of the continuum at different epochs (points show the measurements, and the line is a linear fit).

MJD (1)	Line (2)	λ_0 (3)	Amp (4)	FWHM (5)	v (6)	Flux (7)	S_{cont} (8)	EW (9)
58876.578	MgII	2795±2	0.37±0.04	18.4±1.3	1982±140	13±3	7.1±0.2	2±1
58887.497	MgII	2798±3	0.36±0.06	26.0±2.6	2787±278	18±4	3.3±0.2	6±3
58904.368	MgII	2797±2	0.31±0.02	28.6±0.7	3074±75	16±2	1.5±0.2	11±2
58876.578	FeII	2390±5	0.49±0.05	91±3	–	84±9	9.2±0.5	–
58887.497	FeII	2357±5	0.23±0.06	91±2	–	58±5	4.5±0.2	–
58904.368	FeII	2348±5	0.15±0.03	91±1	–	27±7	1.8±0.3	–

Table 4. Parameters of Lines. Columns as follows: (1) epoch of observations; (2) emission line; (3) central wavelength of Gaussian fit in Å (4) amplitude of Gaussian fit in units of $10^{-15}\text{erg cm}^{-2}\text{s}^{-1}\text{Å}^{-1}$; (5) full width of Gaussian at half-maximum (FWHM) in Å (6) velocity of gas in km s^{-1} ; (7) flux of line in $10^{-15}\text{erg cm}^{-2}\text{s}^{-1}$; (8) flux density of the continuum at the peak of line in $10^{-15}\text{erg cm}^{-2}\text{s}^{-1}\text{Å}^{-1}$; (9) equivalent width in Å.

The total and polarized intensity images are modeled by circular components with Gaussian brightness distributions. Two bright features are apparent at each epoch: the core A0, and a knot K20. We assume that the core is a stationary feature of the jet and calculate parameters of K20 with respect to the core. Parameters of the modeling are given in Table 5.

According to Fig. 10 and Table 5, knot K20 is the most polarized feature of the jet. Fig. 11 shows the separation of K20 from the core as a function of time. According to a linear approximation, K20 moves with a proper motion $\mu = 0.30 \pm 0.04$ mas/yr, which translates into superluminal motion down the jet with apparent speed $\beta_{app} = 12.0 \pm 1.7$ in units of c . Such motion suggests that the ejection¹⁷ of K20 through the VLBI core occurred on MJD 58831±21 (2019 December 13). Fig. 11 also shows the light curve of K20, which reveals a very fast decrease of the knot flux density by a factor of ~ 4 in three months, which corresponds to the timescale of variability of 0.16 ± 0.03 yr, as defined according to Burbidge, Jones, & O’Dell (1974). Applying the formalism proposed by Jorstad et al. (2005), this timescale of variability and the average size of K20 (0.084 ± 0.015 mas according to Table 5) give a value of the Doppler factor of K20 $\delta = 33 \pm 9$. The latter, along with the apparent speed of the knot, allow us to estimate the Lorentz factor, $\Gamma_b = 19 \pm 9$, and viewing angle $\Theta_o = 1.1^\circ \pm 0.6^\circ$ of K20. Using the proper motion and size of K20, we can estimate that during the time of VHE emission the upstream edge of the knot was passing through the centroid of the core. The direction of polarization in K20 is close to the jet direction, which suggests that K20 is most likely a moving shock whose surface is oriented transverse to the jet axis. This is supported by a higher degree of polarization of the knot compared with the core, which implies ordering of the magnetic field as expected by such a shock.

4. Spectral energy distribution modeling

FSRQ gamma-ray emission is usually explained in the framework of an external Compton (EC) model. Moreover, the optical spectroscopy measurements performed during the dimming phase of the emission (see Fig. 8) show a significant increase in flux of FeII + FeIII lines. Since the source emits up to VHE range, the most natural target for EC process is the dust torus (DT) radiation field (see, e.g., Costamante et al. 2018; van den Berg et al. 2019). DT radiation field, contrary to BLR would not absorb strongly the sub-TeV gamma-rays, and thus is the common assumption for the dominating radiation field in the modeling of FSRQs detected at VHE gamma rays. On the other hand the large increase of the optical flux during the gamma-ray

flare can provide as well a significant target for synchrotron-self-Compton (SSC) process. We therefore investigate a scenario in which both SSC and EC processes are possible.

Intriguingly, compared to the low-state spectrum, the investigated synchrotron and gamma-ray peaks are shifted towards higher energies. Similar behavior has been observed also in a few other FSRQs during enhanced states, e.g.: PMN J2345–1555 (Ghisellini et al. 2013), 4C +49.22 (Cutini et al. 2014), PKS 1441+25 (Ahnen et al. 2015; Abeysekara et al. 2015), PKS 1510–089 (D’Ammando et al. 2011), and PKS 0346–27 (Angioni et al. 2019). For most of these cases, however, the peak frequency did not reach beyond 10^{14} Hz. Therefore, the behavior observed in QSO B1420+326, in particular the SED peaking at a few times 10^{14} Hz in optical range during period B, while not being unique is still rarely observed in FSRQs. The peak position traces the electron energy distribution (EED), however, it is also dependent on other physical parameters of the source (e.g. on the beaming).

We model the source in a framework of a simple one-zone model in which a spherical emission region is homogeneously and isotropically filled with an electron distribution and magnetic field. We consider a broken power-law energy distribution of electrons, i.e. $dN_e/d\gamma \propto \gamma^{-p_1}$ for $\gamma_{min} < \gamma < \gamma_b$ and $dN_e/d\gamma \propto \gamma^{-p_2}$ for $\gamma_b < \gamma < \gamma_{max}$. The electrons in the blob are also exposed to an additional, directional radiation field coming from the DT. The model assumes ring geometry of the DT, and thus depends on the distance of the emission region from the black hole. The SED model was generated with *agnpy*¹⁸ (Nigro et al. 2020), which implements the synchrotron and Compton processes following the prescriptions described in Dermer & Menon (2009); Finke (2016). We fix the Lorentz and Doppler factors of the blob to $\Gamma = 40$ and $\delta = 40$, respectively. Note that those values are somewhat larger (in particular the Γ factor of the blob) than the jet parameters estimated using VLBI observations (see Section 3.6). However, the VLBI measurements are performed a few months after the flaring event and trace the later evolution of the blob, thus some change of parameters of the jet might have happened in the meantime (in particular deceleration). The size of the blob is limited by the variability condition. The values that we use in the modeling, $r_b = 3 - 6 \times 10^{16}$ cm, correspond to the light crossing time of 12–24 hrs, of the order of the time scale of the observed variability. We assume that the emission region is located at the distance of $d = 2.5 \times 10^{18}$ cm, i.e. of the order of $\sim \Gamma r_b$. We use the accretion disk luminosity $L_{disk} = 2 \times 10^{46} \text{erg s}^{-1}$ (see Section 3.5) to estimate the size of the BLR and DT following the scaling relations of Ghisellini & Tavecchio (2009). Note that while the optical spectra used in this estimation are not fully simultaneous with the broadband emis-

¹⁷ passage of the centroid of K20 through the centroid of A0

¹⁸ <https://github.com/cosimoNigro/agnpy/>

MJD (1)	Knot (2)	S (3)	R (4)	Θ (5)	a (6)	P (7)	EVPA (8)
58916	A0	0.90 ± 0.06	0.0	–	0.029 ± 0.007	3.5 ± 0.3	110 ± 6
58979	A0	0.52 ± 0.06	0.0	–	0.023 ± 0.007	1.5 ± 0.5	-20 ± 8
59006	A0	0.44 ± 0.05	0.0	–	0.066 ± 0.010	0.8 ± 0.3	78 ± 11
58916	K20	0.46 ± 0.04	0.073 ± 0.018	118 ± 9	0.088 ± 0.014	6.5 ± 0.4	113 ± 7
58979	K20	0.26 ± 0.03	0.118 ± 0.024	120 ± 8	0.096 ± 0.017	5.7 ± 0.3	114 ± 6
59006	K20	0.10 ± 0.02	0.151 ± 0.015	117 ± 8	0.067 ± 0.015	8.3 ± 0.5	91 ± 6

Table 5. Parameters of core A0 and knot K20. Columns of table are: (1) epoch of observation in MJD; (2) designation of knot; (3) flux density, S , in Jy; (4) distance from the core, R , in mas; (5) position angle with respect to the core, Θ , in degrees; (6) FWHM size of knot, a , in mas; (7) degree of polarization, P , in %; and (8) position angle of polarization, EVPA, in degrees. For model parameters, 1σ uncertainties are provided.

sion data used for the modeling, the size of the DT makes the emission quasi-stable at the time scales of years. DT is simulated as a thin ring with a radius of $R_{DT} = 1.1 \times 10^{19}$ cm (3.6 pc). Since the estimated size of the BLR is $R_{BLR} = 4.4 \times 10^{17}$ cm (0.14 pc), the emission region is not affected by the BLR but it is deep in the DT radiation field. We assume that 0.6 of the disk luminosity is reprocessed in the DT radiation.

In order to obtain EED in a self-consistent way we introduce the acceleration parameter ξ , defined such that acceleration gain of electrons is $(dE/dt)_{acc} = \xi cE/R_L$, where c is the speed of light and R_L is the Larmor radius. The maximum energy of the electrons is obtained from comparing the acceleration energy gain with energy losses due to IC (in Thomson regime) cooling:

$$\gamma_{max} = \sqrt{3\xi eB/4\sigma_T u'_{ph}}, \quad (1)$$

where B is the co-moving magnetic field in the blob, e is elementary charge, σ_T is the Thomson cross-section. u'_{ph} is the co-moving energy density of the dominating radiation field. In the case of the parameter sets used in the modeling the dominating radiation field is originating from the DT, however we explicitly check also possible limit from the SSC process. The maximum electron energies are also tested against the dynamical time scale, by comparing the acceleration time scale with the ballistic time scale¹⁹, $T_{bal} \approx r_b/c$ of the blob crossing its size, and against synchrotron energy losses. However, neither of the two processes is dominant in the cases investigated here. Since during T_{bal} the blob crosses its size, it might escape the region in the jet (e.g. a stationary shock) where efficient acceleration occurs. Note that T_{bal} determines also the time scale of adiabatic losses of the electron (at the assumption that the blob distance is $d = r_b\Gamma$).

We also introduce a canonical cooling break (steepening of EED by 1) at the energy where the dominating cooling time scale is equal to the ballistic time scale, T_{bal} :

$$\gamma_b = 3m_e c^2 / 4\sigma_T u'_{ph} r_b, \quad (2)$$

where m_e is the electron mass. In order not to overshoot the X-ray flux with IC photons and still be able to explain the gamma-ray emission during the periods B, C and D it is necessary to assume that the EED starts at $\gamma_{min} > 1$. We apply values of $\gamma_{min} = 10 - 15$ in the modeling, while for period A we use $\gamma_{min} = 1$. We then tune the magnetic field B and the energy density of the electrons u'_e to reproduce the levels of synchrotron and IC emission. The index of EED before the break is selected to roughly reproduce the spectral shape in IR-UV (except of period D) and gamma-ray bands. The resulting value $p_1 = 1.7 - 2$, is close to the canonical non-relativistic value of 2 (see, e.g., Drury

¹⁹ also called light crossing time scale

1983). The location of the valley between the peaks is most sensitive to the maximum γ factor of the electrons and the onset of the IC peak. The maximum energies of the electrons are tuned by the acceleration parameter ξ (see Eq. 1) with an additional constraint from the VHE gamma-ray spectrum. The depth of the valley is modified additionally by the SSC component. By tuning the compactness of the blob (i.e. varying the radius of the blob within a factor of 2 with simultaneous keeping the same total power in electrons that fixes the synchrotron and EC emission at roughly the same level), which affects the SSC emission, we fit the depth of the dip in periods B, C and D. Since in all the studied energy bands the emission during the whole investigated period was significantly larger than the historical measurements we neglect the possible low-state emission of the source in the modeling. The broadband spectra obtained from the modeling are compared with measured ones in Fig. 12. The corresponding evolution of EED is shown in Fig. 13. Parameters of the modeling are shown in Table 6.

It should be stressed that, mainly due to fixing the Doppler factor, those parameters are not uniquely determined (see, e.g., Ahnen et al. 2017b). For example, assuming δ and Γ motivated by VLBI measurements, a similar fit to the data can be achieved, however, with the size of the emission region compressed by about an order of magnitude in periods A, C and D. They allow us however to trace the relative evolution of the parameters with the assumption that the beaming did not change during the flare. The gamma-ray spectrum in the modeling is reproduced by nearly solely the EC process. The high spectral variability of the X-ray emission is naturally explained by three processes that contribute to it: mainly the EC and SSC emission, with a partial component from the highest-energies synchrotron radiation during period C.

Due to its simplicity the modeling has some caveats. The radio emission is underestimated due to pronounced synchrotron self absorption in the model curve. Such emission is often attributed to a larger-scale jet, rather than the blob. It should be noted however that during the 2020 high state the radio emission was at higher level than in historical measurements, and also the emission has shown some variability, therefore it should be also at least partially associated with the high state. It is plausible that, due to evolution of the flare, low-energy electrons from the blob escape to the large scale jet without being cooled completely. Such an enhancement of the EED in the large scale jet during the high state would explain higher radio emission. In addition such escape of high energy particles along the jet would naturally explain the new component appearing in VLBI follow-up of the flare.

In period C (and partially also in period D) the X-ray data show a clear valley between the two peaks. The shape of the low-energy (i.e. falling) part of the valley in this period is not fully

Period	δ	r_b [cm]	ξ	B [G]	U'_e [10^{48} erg]	p_1	γ_{\min}	p_2	γ_{break}	γ_{\max}	u'_e [erg cm $^{-3}$]	u'_e/u'_B
A	40	6.16×10^{16}	0.3×10^{-7}	0.70	1.18	1.7	1	2.7	63	6900	1.2×10^{-3}	0.06
B	40	3.70×10^{16}	0.3×10^{-7}	0.95	1.76	1.8	15	2.8	104	8000	8.3×10^{-3}	0.23
C	40	3.08×10^{16}	3.0×10^{-7}	0.83	2.12	2.0	10	3.0	125	23700	17.3×10^{-3}	0.63
D	40	3.08×10^{16}	6.0×10^{-7}	0.55	2.35	2.0	10	3.0	125	27300	19.2×10^{-3}	1.6

Table 6. Parameters used for the modeling: Doppler factor δ ($\Gamma = \delta$ is assumed), co-moving size of the emission region r_b , acceleration parameter ξ , magnetic field B , total energy of electron U'_e , EED: slope before the break: p_1 , minimum Lorentz factor γ_{\min} , slope after the break p_2 , the Lorentz factor of the break γ_{break} , maximum Lorentz factor γ_{\max} , electron energy density u'_e , energy equipartition u'_e/u'_B . Free parameters of the model and derived parameters are put on the left and right side of the double vertical line respectively

reproduced by the model. This part of the SED is strongly dependent on the shape of the high-energy tail of the EED which is also constrained by the highest energy gamma rays. The simplifications in the modeling (homogeneous region, no non-stationary processes modifying EED within the considered period, resulting sharp cut-off of the EED) do not allow us to realistically model the full shape of the valley. The SED in this period might be also affected by fast variability.

The slope of the spectrum is not accurately modeled in all the cases. In particular in period D (and partially also in period C) the optical range would require softer electron distribution than gamma-ray range. In particular in period C the NIR data are slightly overshooting the model suggesting a softer spectrum. This might be connected with fast variability of the source, or with additional emission of the population of partially cooled particles from the previous phases of the flare.

Despite those caveats it is interesting to see that the obtained model parameters provide a self-consistent description of the main features of the emission during different phases of the flare. Comparing period B to period A modeling suggests a compression of the emission region coincident with the increase of the minimum Lorentz factor of the electrons and a mild increase of the magnetic field density and the total energy stored in electrons.

The increased γ_{\min} factor needed in the modeling (see also Katarzyński et al. 2006) might point to a two-stage acceleration process. First, injection of particles with such minimum Lorentz factor has to occur, e.g., due to acceleration in a small potential drop due to reconnection of magnetic fields (see, e.g., Lazarian et al. 2015; Comisso & Sironi 2019). Then a second process (e.g., Fermi second order acceleration) would boost the particles to a power-law spectrum up to maximal gamma factors of γ_{\max} . The acceleration coefficient ξ has a rather small value, of the order of 10^{-7} . The value of ξ in the modeling increases by an order of magnitude in period C in order to explain the VHE gamma-ray emission. Such small values are needed to saturate the acceleration process with EC energy losses in order not to increase too much γ_{\max} and in turn not to overshoot the X-ray emission by synchrotron component. As shown in the modeling such acceleration would be still efficient enough to explain the observed optical and HE flare. A natural explanation for such low values of ξ is a second order Fermi process with non-relativistic scattering centers accelerating electrons in the emission region. During the period D the VHE emission requires a further small increase of the ξ parameter coincident with lower magnetic field in order not to overshoot the soft X-ray flux with the synchrotron component.

5. Discussion and conclusions

Observations of QSO B1420+326 with MAGIC during the enhanced state allowed us to add a new member to the sparse fam-

ily of the FSRQs emitting in VHE range. The observations were performed during an impressive flare, with the flux of both SED peaks enhanced by about two orders of magnitude with respect to the low state. Monitoring observations of the source and a massive MWL campaign provided us a dataset that was used to trace the evolution of the EED during the flare. Interestingly, the synchrotron spectrum in the optical range during the flare (in particular period B) is hard. Comparing to historical data, both low- and high-energy peaks shifted by at least two orders of magnitude in frequency, such large shift being rare for a FSRQ object. Shifts of the peaks towards higher energies during high states is a behavior commonly observed in a sister class of objects – BL Lacs. The spectra are Compton dominated, which is typical for FSRQs. However, the dominance during the peak of the flare is just a factor of a few.

Similarly to other VHE-detected FSRQs, we get a satisfactory description of the two broad peaks of the SED as the synchrotron and EC on DT radiation field. The valley between the peaks is well constrained by the X-ray data, and we use it to track the changes of the compactness of the blob during the evolution of the high state. The modeling scenario is self-consistent in the sense of the shape of the EED being determined by the balance of acceleration and cooling processes. The variability of the emission between different phases of the enhanced state is explained mainly by a combination of variations of the compactness of the emission region, the minimal injection energy of electrons and increase of the acceleration parameters. In addition to achieve a satisfactory fit coincident small variations of the magnetic field, total energy stored in electrons, and injection slope has been assumed.

The optical spectroscopy observations revealed a prominent MgII line, that does not show flux variability exceeding the uncertainties of the measurements. We explain this as the line being produced within a canonical BLR, and so has a much longer timescale of variability. Therefore, the MgII line is a good proxy for estimating the accretion disk luminosity at 2×10^{46} erg s $^{-1}$. Additionally, a broad FeII bump has been observed, with the luminosity increasing with the increase of the optical continuum emission. The fast variability of the FeII bump suggests that it originates in a much smaller region (possibly located close to the jet axis) than the regular BLR. Moreover, since the flux of FeII bump correlates with the synchrotron continuum, the bump should be produced farther from the black hole in the vicinity of the jet. Additionally, the shift of the bump to the blue side could be explained if it is produced in a wind surrounding the jet. This suggests a possible interaction of the jet with a FeII-emitting cloud.

Optical polarimetry, that started a few days after optical peak, shows a very low polarization and smooth EVPA rotation. This makes QSO B1420+326 another FSRQ in which VHE gamma-ray emission is detected contemporaneous to EVPA rotations. Intriguingly, the VLBI observations in the follow up of

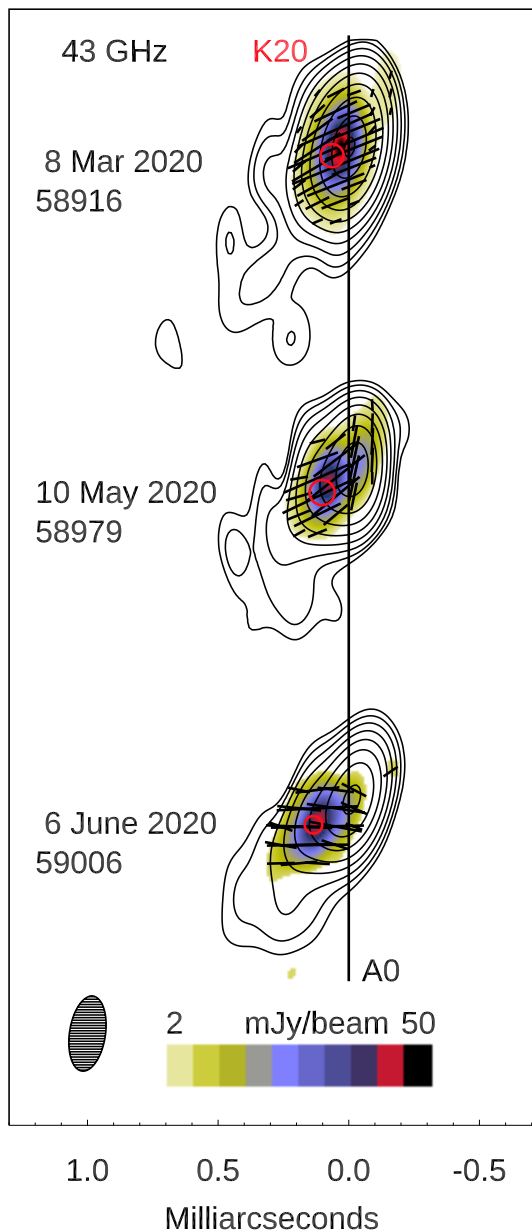


Fig. 10. Total (contours) and polarized (color scale) intensity maps of QSO B1420+326 obtained with the VLBA at 43 GHz; the peak total intensity is 1.14 Jy/beam; the beam is displayed in the bottom left corner; the contours are 0.25, 0.5, 1,...,64, 90% of the peak total intensity. Linear segments within images show direction of polarization, the black vertical line indicates the position of the core, A0, and red circles mark positions of knot K20; 1 mas corresponds to 7.29 pc. Note that the polarized flux intensities on May 10 and June 6 are multiplied by factors of 3 and 5, respectively, to reveal locations of peaks of polarized flux intensity, which are 15 mJy/beam and 9.5 mJy/beam, respectively, for the May 10 (MJD=58979) and June 6 (MJD=59006) images.

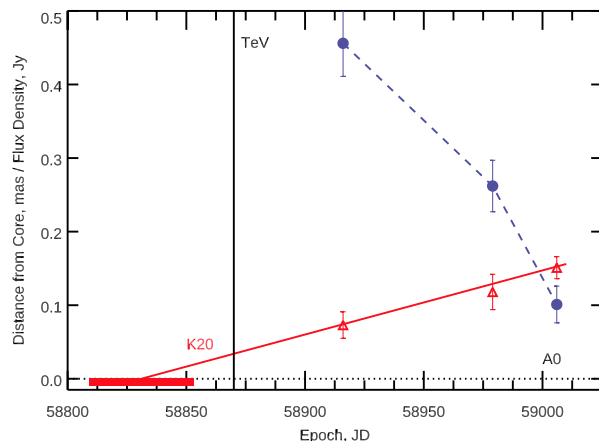


Fig. 11. Separation of K20 from the core with time (red triangles) according to modeling; the red line represents a linear approximation of the motion. Blue circles and dashed line correspond to the light curve of K20 at 43 GHz; the black vertical line indicates the time of the VHE event.

the flare show an emission of a superluminal radio knot contemporaneous with the high gamma-ray state. Similar association for VHE gamma-ray emission + EVPA rotation + VLBI component ejection has been previously suggested also for another FSRQ PKS 1510–089 (Ahnen et al. 2017a).

The detection of QSO B1420+326 in the VHE gamma-ray range and the extensive monitoring campaign during this event add another piece to solving the puzzle of the origin of the highest energy emission of FSRQ objects. It is interesting that some of the emission features associated with these observations of QSO B1420+326 are similar to observations of other FSRQs, in particular of PKS 1510–089, so far the most thoroughly studied FSRQ in the VHE range. QSO B1420+326 might be a cousin of PKS 1510–089, twice as distant but intrinsically more luminous.

Acknowledgements.

We would like to dedicate this paper to the memory of our friend and colleague, Dr. Valeri Larionov (1950–2020), who enthusiastically contributed to this and many other projects aimed at understanding blazars.

We would like to thank the Instituto de Astrofísica de Canarias for the excellent working conditions at the Observatorio del Roque de los Muchachos in La Palma. The financial support of the German BMBF and MPG; the Italian INFN and INAF; the Swiss National Fund SNF; the ERDF under the Spanish MINECO (FPA2017-87859-P, FPA2017-85668-P, FPA2017-82729-C6-2-R, FPA2017-82729-C6-6-R, FPA2017-82729-C6-5-R, AYA2015-71042-P, AYA2016-76012-C3-1-P, ESP2017-87055-C2-2-P, FPA2017-90566-REDC); the Indian Department of Atomic Energy; the Japanese ICRR, the University of Tokyo, JSPS, and MEXT; the Bulgarian Ministry of Education and Science, National RI Roadmap Project DOI-268/16.12.2019 and the Academy of Finland grant nr. 320045 is gratefully acknowledged. This work was also supported by the Spanish Centro de Excelencia “Severo Ochoa” SEV-2016-0588 and SEV-2015-0548, the Unidad de Excelencia “María de Maeztu” MDM-2014-0369 and the “la Caixa” Foundation (fellowship LCF/BQ/PI18/11630012), by the Croatian Science Foundation (HrZZ) Project IP-2016-06-9782 and the University of Rijeka Project 13.12.1.3.02, by the DFG Collaborative Research Centers SFB823/C4 and SFB876/C3, the Polish National Research Centre grant UMO-2016/22/M/ST9/00382 and by the Brazilian MCTIC, CNPq and FAPERJ. The Fermi-LAT Collaboration acknowledges generous ongoing support from a number of agencies and institutes that have supported both the development and the operation of the LAT, as well as scientific data analysis. These include the National Aeronautics and Space Administration and the Department of Energy in the United States; the Commissariat à l’Énergie Atomique and the Centre National de la Recherche Scientifique/Institut National de Physique Nucléaire et de Physique des Particules in France; the Agenzia Spaziale Italiana and the Istituto Nazionale di Fisica Nucleare in Italy; the Ministry of Education, Culture, Sports, Science and Technology (MEXT), High Energy Accelerator Research Organization (KEK), and Japan Aerospace Exploration Agency (JAXA) in Japan; and the

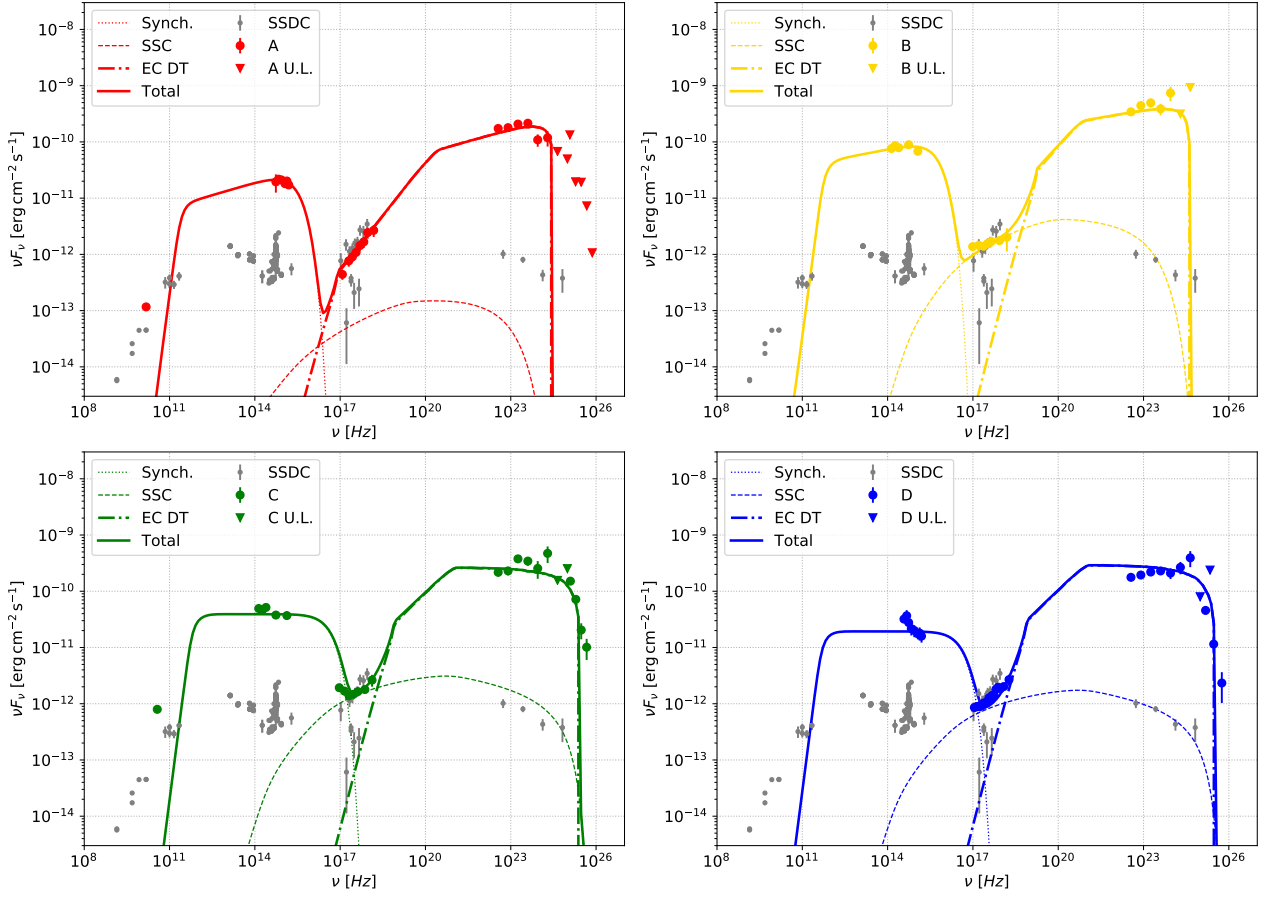


Fig. 12. Multiwavelength SED of QSO B1420+326 in the four periods A – before the flare, B – optical flare, C – VHE gamma-ray flare, D – after the flare and archival data (gray). Different radiation processes are shown with different line styles: dotted lines – synchrotron, dashed – SSC, dot-dashed – EC, solid – sum of components. Model lines are corrected for EBL absorption according to Domínguez et al. (2011).

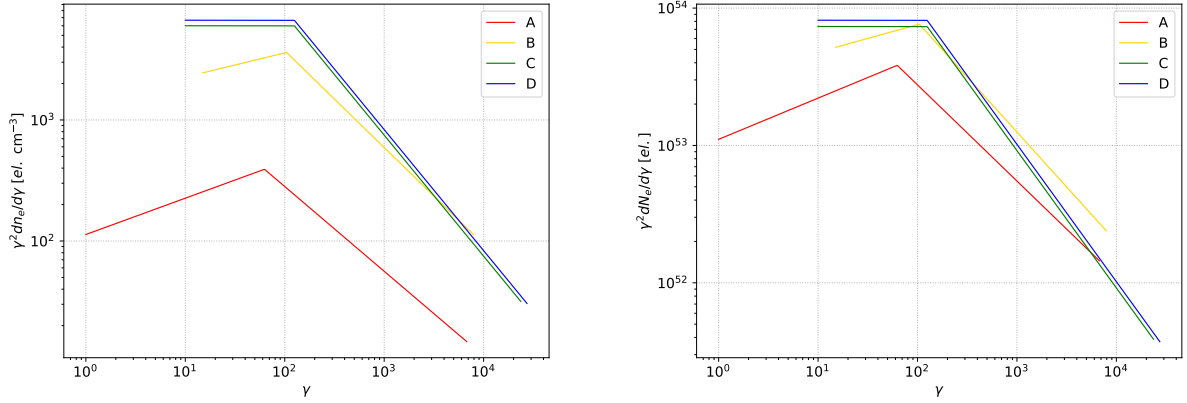


Fig. 13. Evolution of the EED in the frame of the blob: energy density (left) and total energy integrated over the blob (right). Different line colors represent different stages of the flare.

K. A. Wallenberg Foundation, the Swedish Research Council, and the Swedish National Space Board in Sweden. Additional support for science analysis during the operations phase is gratefully acknowledged from the Istituto Nazionale di Astrofisica in Italy and the Centre National d'Etudes Spatiales in France. This work was performed in part under DOE Contract DE-AC02-76SF00515. This publication makes use of data obtained at the Metsähovi Radio Observatory, operated by Aalto University in Finland. This research has made use of data from the OVRO 40-m monitoring program Richards et al. (2011) which is supported in part by NASA grants NNX08AW31G, NNX11A043G, and NNX14AQ89G and NSF grants AST-0808050 and AST-1109911. This study was based in part on observations conducted using the 1.8m Perkins Telescope Observatory

(PTO) in Arizona, which is owned and operated by Boston University. The research at Boston University was supported in part by NASA Fermi GI program grants 80NSSC17K0649, 80NSSC19K1504, and 80NSSC19K1505. We thank the ASAS-SN team for making their data publicly available. The VLBA is an instrument of the National Radio Astronomy Observatory. The National Radio Astronomy Observatory is a facility of the National Science Foundation operated by Associated Universities, Inc. This work made use of the Lowell Discovery Telescope (formerly Discovery Channel Telescope) at Lowell Observatory. Lowell is a private, nonprofit institution dedicated to astrophysical research and public appreciation of astronomy and operates the LDT in partnership with Boston University, the University of Maryland, the University of Toledo, Northern Arizona

University, and Yale University. We acknowledge support by Bulgarian National Science Fund under grant DN18-10/2017 and National RI Roadmap Projects DOI-277/16.12.2019 and DOI-268/16.12.2019 of the Ministry of Education and Science of the Republic of Bulgaria.

References

- H. E. S. S. Collaboration, Abdalla, H., Adam, R., et al. 2020, *A&A*, 633, A162
- Abdollahi, S., Acero, F., Ackermann, M., et al. 2020, *ApJS*, 247, 33
- Abeyskara, A. U., Archambault, S., Archer, A., et al. 2015, *ApJ*, 815, L22
- MAGIC Collaboration, Acciari, V. A., Ansoldi, S., et al. 2018, *A&A*, 619, A159
- Acero, F., Ackermann, M., Ajello, M., et al. 2016, *ApJS*, 223, 26
- Planck Collaboration, Ade, P. A. R., Aghanim, N., et al. 2014, *A&A*, 571, A28
- Ahnen, M. L., Ansoldi, S., Antonelli, L. A., et al. 2015, *ApJ*, 815, L23
- Ahnen, M. L., Ansoldi, S., Antonelli, L. A., et al. 2017, *A&A*, 603, A29
- Ahnen, M. L., Ansoldi, S., Antonelli, L. A., et al. 2017, *A&A*, 603, A31
- Ajello, M., Atwood, W. B., Baldini, L., et al. 2017, *ApJS*, 232, 18
- Albareti, F. D., Allende Prieto, C., Almeida, A., et al. 2017, *ApJS*, 233, 25
- Aleksić, J., Antonelli, L. A., Antoranz, P., et al. 2011, *ApJ*, 730, L8
- Aleksić, J., Ansoldi, S., Antonelli, L. A., et al. 2014, *A&A*, 569, A46
- Aleksić, J., Ansoldi, S., Antonelli, L. A., et al. 2016, *Astroparticle Physics*, 72, 61
- Aleksić, J., Ansoldi, S., Antonelli, L. A., et al. 2016, *Astroparticle Physics*, 72, 76
- Angioni, R. 2019, *The Astronomer's Telegram* 12942, 1
- Angioni, R., Nesci, R., Finke, J. D., et al. 2019, *A&A*, 627, A140
- Atwood, W. B., Abdo, A. A., Ackermann, M., et al. 2009, *ApJ*, 697, 1071
- Atwood, W., Albert, A., Baldini, L., et al. 2013, *arXiv:1303.3514*
- Baldwin, J. A., Ferland, G. J., Korista, K. T., et al. 2004, *ApJ*, 615, 610
- Ben Bekhti, N., Flöer, L., Keller, R., et al. 2016, *A&A*, 594, A116
- van den Berg, J. P., Böttcher, M., Domínguez, A., et al. 2019, *ApJ*, 874, 47
- Bessell, M. S., Castelli, F., & Plez, B. 1998, *A&A*, 333, 231
- Bianchi, L., Efremova, B., Herald, J., et al. 2011, *MNRAS*, 411, 2770
- Boller, T., Freyberg, M. J., Trümper, J., et al. 2016, *A&A*, 588, A103
- Breeveld, A. A., Curran, P. A., Hoversten, E. A., et al. 2010, *MNRAS*, 406, 1687
- Burbidge, G. R., Jones, T. W., & O'Dell, S. L. 1974, *ApJ*, 193, 43
- Burrows D. N., Hill, J. E., Nousek, J. A., et al. 2005, *SSRv*, 120, 165
- Cardelli, J. A., Clayton, G. C.; Mathis, J. S. 1989, *ApJ*, 345, 245
- Carrasco, L.; Hernandez-Utrera, O.; Vazquez, S., Maya, Y. D.; Carrasco, E.; Pedraza, J.; Castillo, E.; Escobedo, G.; Devaraj; Luna, A. 2017, *RMxAA*, v.53, pp.497-506.
- Cash, W. 1979, *ApJ*, 228, 939
- Ceribella, G., D'Amico, G., Dazzi, F., et al. 2019, 36th International Cosmic Ray Conference (ICRC2019), 645
- Ciprini, S. 2018, *The Astronomer's Telegram* 12277, 1
- Ciprini, S., & Cheung, C. C. 2020, *The Astronomer's Telegram* #13382
- Cohen, M. Weaton, W. A., Megeath, S. F. 2003, *AJ*, v.126, pp.1090-1096.
- Comisso, L., & Sironi, L. 2019, *ApJ*, 886, 122
- Condon, J. J., Cotton, W. D., Greisen, E. W., et al. 1998, *AJ*, 115, 1693
- Costamante, L., Cutini, S., Tosti, G., et al. 2018, *MNRAS*, 477, 4749
- Covino, S., Zerbi, F. M., Chincarini, G., et al. 2004, *SPIE*, 5492, 1613
- Cutini, S., Ciprini, S., Orienti, M., et al. 2014, *MNRAS*, 445, 4316
- Dermer, C. D. & Menon, G. 2009, *High Energy Radiation from Black Holes: Gamma Rays, Cosmic Rays, and Neutrinos* by Charles D. Dermer and Govind Menon. Princeton University Press, November 2009.
- D'Ammando, F., Raiteri, C. M., Villata, M., et al. 2011, *A&A*, 529A, 145
- D'Ammando, F., Raiteri, C. M., Villata, M., et al. 2019, *MNRAS*, 490, 5300
- D'Ammando, F., Fugazza, D., Covino, S. 2020, *The Astronomer's Telegram* 13428
- Domínguez, A., Primack, J. R., Rosario, D. J., et al. 2011, *MNRAS*, 410, 2556
- Drury, L. O. 1983, *Reports on Progress in Physics*, 46, 973
- Evans, P. A., Beardmore, A. P., Page, K. L., et al. 2009, *MNRAS*, 397, 1177
- Finke, J. D. 2016, *ApJ*, 830, 94
- Fruck, C., & Gaug, M. 2015, *European Physical Journal Web of Conferences*, 89, 02003
- García, J. R., Dazzi, F., Häfner, D., et al. 2014, 33rd International Cosmic Ray Conference, *arXiv:1404.4219*
- Gehrels, N., Chincarini, G., Giommi, P., et al. 2004, *ApJ*, 611, 1005
- Ghisellini, G., & Tavecchio, F. 2009, *MNRAS*, 397, 985
- Ghisellini, G., Tavecchio, F., Foschini, L., et al. 2013, *MNRAS*, 432, L66
- Ghisellini, G., Tavecchio, F., Maraschi, L., et al. 2014, *Nature*, 515, 376
- Gregory, P. C., Scott, W. K., Douglas, K., et al. 1996, *ApJS*, 103, 427
- Jansen, F., Lumb, D., Altieri, B., et al. 2001, *A&A*, 365, L1
- Jester, S., Schneider, D. P., Richards, G. T., et al. 2005, *AJ*, 130, 873
- Jorstad, S. G., Marscher, A. P., Lister, M. L., et al. 2005, *AJ*, 130, 1418
- Jorstad, S. G., Marscher, A. P., Larionov, V. M., et al. 2010, *ApJ*, 715, 362
- Jorstad, S. G., Marscher, A. P., Morozova, D. A., et al. 2017, *ApJ*, 846, 98
- Ghisellini, G. 2016, *Galaxies*, 4, 36
- Healey, S. E., Romani, R. W., Taylor, G. B., et al. 2007, *ApJS*, 171, 61
- Henden A. A., Templeton M., Terrell D., Smith T. C., Levine S., Welch D., 2016, *yCat*, II/336
- Hewett, P. C., & Wild, V. 2010, *MNRAS*, 405, 2302
- Jackson, N., Battye, R. A., Browne, I. W. A., et al. 2007, *MNRAS*, 376, 371
- Katarzyński, K., Ghisellini, G., Tavecchio, F., et al. 2006, *MNRAS*, 368, L52
- Kharinov, M. A. 2020, *The Astronomer's Telegram* #13479
- Kochanek, C. S., Shappee, B. J., Stanek, K. Z., et al. 2017, *PASP*, 129, 104502
- Larionov, V. M., Jorstad, S. G., Marscher, A. P., et al. 2008, *A&A*, 492, 389
- Lazarian, A., Eyink, G. L., Vishniac, E. T., et al. 2015, *Magnetic Fields in Diffuse Media*, 311
- Lindfors, E. 2015, *Extragalactic Jets from Every Angle*, 27
- Liu, H. T., & Bai, J. M. 2006, *ApJ*, 653, 1089
- Lott, B., Escande, L., Larsson, S., et al. 2012, *A&A*, 544, A6
- Marchini A., Bonnoli, G., Bellizzi, L., et al. 2019, *ATel*, 12914, 1
- Mattox, J. R., Bertsch, D. L., Chiang, J., et al. 1996, *ApJ*, 461, 396
- Meyer, M., Scargle, J. D., & Blandford, R. D. 2019, *ApJ*, 877, 39
- Minev, M., Kurtenkov, A., Ovcharov, E. 2020, *The Astronomer's Telegram* 13421
- Mirzoyan, R. 2020, *The Astronomer's Telegram* #13412
- van Moorsel, G., Kemball, A., & Greisen, E. 1996, in *Astronomical Data Analysis Software and Systems V*, eds. G.H. Jacoby and J. Barnes, *A.S.P. Conference Series*, 101, 37
- Munari U., 2012, *JAVSO*, 40, 582
- Myers, S. T., Jackson, N. J., Browne, I. W. A., et al. 2003, *MNRAS*, 341, 1
- Nigro, C., Sitarek, J., Craig M. & Gliwny, P. (2020, September 28). *agnpy: modelling Active Galactic Nuclei radiative processes with python*. Zenodo. <http://doi.org/10.5281/zenodo.4055176>
- Oh, K., Koss, M., Markwardt, C. B., et al. 2018, *ApJS*, 235, 40
- Ovcharov, E. P., Kurtenkov, A., Metodjeva, Y., et al. 2014, *Bulgarian Astronomical Journal*, 21, 19
- Poole, T. S., Breeveld, A. A., Page, M. J., et al. 2008, *MNRAS*, 383, 627
- Fallah Ramazani, V. Bonnoli, G., D'Ammando, F., Cerruti, M., Righi, C., Sitarek, J. 2020, *The Astronomers' Telegram* 13417
- Planck Collaboration, Aghanim, N., Akrami, Y., et al. 2020, *A&A*, 641, A6. doi:10.1051/0004-6361/201833910
- Rani, B., Jorstad, S. G., Marscher, A. P., et al. 2018, *ApJ*, 858, 80
- Richards, J. L., Max-Moerbeck, W., Pavlidou, V., et al. 2011, *ApJS*, 194, 29
- Rolke, W. A., López, A. M., & Conrad, J. 2005, *NIM A*, 551, 493
- Roming, P. W. A., Kennedy, T. E., Mason, K. O., et al., 2005, *SSRv*, 120, 95
- Sambruna, R. M., Maraschi, L., & Urry, C. M. 1996, *ApJ*, 463, 444
- Schlafly, E. F., & Finkbeiner, D. P. 2011, *ApJ*, 737, 103
- Shappee, B. J., Prieto, J. L., Grupe, D., et al. 2014, *ApJ*, 788, 48
- Shayduk, M., 2013, 33rd International Cosmic Ray Conference, 3000, *astro-ph.IM/1307.4939*
- Shepherd, M. C. 1997, in *ASP Conf. Proc., Astronomical Data Analysis Software and Systems VI*, ed. G. Hunt & H. E. Payne (San Francisco: ASP), 125, 77
- Srivastava, M. K., Janra, M., Dixit, V., et al. 2018, *Proc. SPIE*, 107024I
- Stanek, K. Z., Kochanek, C. S., Thompson, T. A., et al. 2017, *The Astronomer's Telegram*, 11110
- Teräsraanta, H., Tornikoski, M., Mujunen, A. et al. 1998, *A&AS*, 132, 305
- Vacca, W.D., Cushing, M.C., and Rayner, J.T. 2002, *arXiv:astro-ph/0211255v1*
- Vanden Berk, D.E., Richards, G.T., and Bauer, A. 2001, *AJ*, 122, 549
- Voges, W., Aschenbach, B., Boller, T., et al. 1999, *A&A*, 349, 389
- White, R. L., Becker, R. H., Helfand, D. J., et al. 1997, *ApJ*, 475, 479
- Wilms J., Allen A., McCray R., 2000, *ApJ*, 542, 914
- Wright, E. L., Eisenhardt, P. R. M., Mainzer, A. K., et al. 2010, *AJ*, 140, 1868
- Wood, M., Caputo, R., Charles, E., et al. 2017, 35th International Cosmic Ray Conference (ICRC2017), 824
- Vaughan, S., Edelson, R., Warwick, R. S., et al. 2003, *MNRAS*, 345, 1271
- Zacharias, M., Dominis Prestero, D., Jankowsky, F., et al. 2019, *Galaxies*, 7, 41
- Zanin, R., Carmona, E., Sitarek, J., et al., 2013, *Proc of 33rd ICRC, Rio de Janeiro, Brazil*, Id. 773
- Zerbi, R. M., Chincarini, G., Ghisellini, G., et al. 2001, *AN*, 322, 275

- ¹ Inst. de Astrofísica de Canarias, E-38200 La Laguna, and Universidad de La Laguna, Dpto. Astrofísica, E-38206 La Laguna, Tenerife, Spain
- ² Università di Udine and INFN Trieste, I-33100 Udine, Italy
- ³ National Institute for Astrophysics (INAF), I-00136 Rome, Italy
- ⁴ ETH Zürich, CH-8093 Zürich, Switzerland
- ⁵ Institut de Física d'Altes Energies (IFAE), The Barcelona Institute of Science and Technology (BIST), E-08193 Bellaterra (Barcelona), Spain
- ⁶ Japanese MAGIC Group: Institute for Cosmic Ray Research (ICRR), The University of Tokyo, Kashiwa, 277-8582 Chiba, Japan
- ⁷ Technische Universität Dortmund, D-44221 Dortmund, Germany
- ⁸ Croatian MAGIC Group: University of Zagreb, Faculty of Electrical Engineering and Computing (FER), 10000 Zagreb, Croatia
- ⁹ IPARCOS Institute and EMFTEL Department, Universidad Complutense de Madrid, E-28040 Madrid, Spain
- ¹⁰ Centro Brasileiro de Pesquisas Físicas (CBPF), 22290-180 URCA, Rio de Janeiro (RJ), Brazil
- ¹¹ University of Lodz, Faculty of Physics and Applied Informatics, Department of Astrophysics, 90-236 Lodz, Poland
- ¹² Università di Siena and INFN Pisa, I-53100 Siena, Italy
- ¹³ Deutsches Elektronen-Synchrotron (DESY), D-15738 Zeuthen, Germany
- ¹⁴ Università di Padova and INFN, I-35131 Padova, Italy
- ¹⁵ INFN MAGIC Group: INFN Sezione di Torino and Università degli Studi di Torino, 10125 Torino, Italy
- ¹⁶ Max-Planck-Institut für Physik, D-80805 München, Germany
- ¹⁷ Università di Pisa and INFN Pisa, I-56126 Pisa, Italy
- ¹⁸ Universitat de Barcelona, ICCUB, IEEC-UB, E-08028 Barcelona, Spain
- ¹⁹ Armenian MAGIC Group: A. Alikhanyan National Science Laboratory
- ²⁰ Centro de Investigaciones Energéticas, Medioambientales y Tecnológicas, E-28040 Madrid, Spain
- ²¹ INFN MAGIC Group: INFN Sezione di Bari and Dipartimento Interateneo di Fisica dell'Università e del Politecnico di Bari, 70125 Bari, Italy
- ²² Croatian MAGIC Group: University of Rijeka, Department of Physics, 51000 Rijeka, Croatia
- ²³ Universität Würzburg, D-97074 Würzburg, Germany
- ²⁴ Finnish MAGIC Group: Finnish Centre for Astronomy with ESO, University of Turku, FI-20014 Turku, Finland
- ²⁵ Departament de Física, and CERES-IEEC, Universitat Autònoma de Barcelona, E-08193 Bellaterra, Spain
- ²⁶ Armenian MAGIC Group: ICRArNet-Armenia at NAS RA
- ²⁷ Croatian MAGIC Group: University of Split, Faculty of Electrical Engineering, Mechanical Engineering and Naval Architecture (FESB), 21000 Split, Croatia
- ²⁸ Croatian MAGIC Group: Josip Juraj Strossmayer University of Osijek, Department of Physics, 31000 Osijek, Croatia
- ²⁹ Japanese MAGIC Group: Department of Physics, Kyoto University, 606-8502 Kyoto, Japan
- ³⁰ Japanese MAGIC Group: Department of Physics, Tokai University, Hiratsuka, 259-1292 Kanagawa, Japan
- ³¹ Saha Institute of Nuclear Physics, HBNI, 1/AF Bidhannagar, Salt Lake, Sector-1, Kolkata 700064, India
- ³² Inst. for Nucl. Research and Nucl. Energy, Bulgarian Academy of Sciences, BG-1784 Sofia, Bulgaria
- ³³ Finnish MAGIC Group: Astronomy Research Unit, University of Oulu, FI-90014 Oulu, Finland
- ³⁴ Croatian MAGIC Group: Ruđer Bošković Institute, 10000 Zagreb, Croatia
- ³⁵ INFN MAGIC Group: INFN Sezione di Perugia, 06123 Perugia, Italy
- ³⁶ INFN MAGIC Group: INFN Roma Tor Vergata, 00133 Roma, Italy
- ³⁷ now at University of Innsbruck
- ³⁸ also at Port d'Informació Científica (PIC) E-08193 Bellaterra (Barcelona) Spain
- ³⁹ also at Dipartimento di Fisica, Università di Trieste, I-34127 Trieste, Italy
- ⁴⁰ Max-Planck-Institut für Physik, D-80805 München, Germany
- ⁴¹ also at INAF Trieste and Dept. of Physics and Astronomy, University of Bologna
- ⁴² Japanese MAGIC Group: Institute for Cosmic Ray Research (ICRR), The University of Tokyo, Kashiwa, 277-8582 Chiba, Japan
- ⁴³ ASI Space Science Data Center, Via del Politecnico, snc. I-00133 Rome - Italy
- ⁴⁴ INFN - Roma Tor Vergata, Via della Ricerca Scientifica, 1. I-00133 Rome - Italy
- ⁴⁵ INAF - IRA Bologna, Via P. Gobetti 101, I-40129, Bologna, Italy
- ⁴⁶ Istituto Nazionale di Fisica Nucleare, Sezione di Perugia, I-06123 Perugia, Italy
- ⁴⁷ Naval Research Laboratory, Washington, DC 20375, USA
- ⁴⁸ INAF - Istituto di Astrofisica e Planetologia Spaziali, Via Fosso del Cavaliere, 100 I-00133 Rome, Italy
- ⁴⁹ Physical Research Laboratory, Ahmedabad, India
- ⁵⁰ Institute of Astronomy and NAO, Bulgarian Academy of Sciences, 72 Tsarigradsko Shose Blvd., 1784 Sofia, Bulgaria
- ⁵¹ Department of Astronomy, Faculty of Physics, University of Sofia, BG-1164 Sofia, Bulgaria
- ⁵² Università di Siena, I-53100, Siena, Italy
- ⁵³ Instituto Nacional de Astrofísica, Óptica & Electrónica Tonantzintla, Puebla, Mexico.
- ⁵⁴ Aalto University Metsähovi Radio Observatory, Metsähovintie 114, FIN-02540 Kylmälä, Finland
- ⁵⁵ Aalto University Department of Electronics and Nanoengineering, P.O. Box 15500, FIN-00076 Aalto, Finland
- ⁵⁶ Finnish Centre for Astronomy with ESO (FINCA), University of Turku, Vesilinnantie 5, FIN-20014 University of Turku, Finland
- ⁵⁷ Institute for Astrophysical Research, Boston University, 725 Commonwealth Avenue, Boston, MA 02215
- ⁵⁸ Astronomical Institute, St. Petersburg University, Universitetskij Pr. 28, Petrodvorets, 198504 St. Petersburg, Russia
- ⁵⁹ Pulkovo Observatory, St.-Petersburg, Russia
- ⁶⁰ Crimean Astrophysical Observatory, Russia
- ⁶¹ Owens Valley Radio Observatory, California Institute of Technology, Pasadena, CA 91125, USA
- ⁶² Institute of Astrophysics, Foundation for Research and Technology-Hellas, GR-71110 Heraklion, Greece,
- ⁶³ Department of Physics, Univ. of Crete, GR-70013 Heraklion, Greece
- ⁶⁴ Departamento de Astronomía, Universidad de Chile, Camino El Observatorio 1515, Las Condes, Santiago, Chile
- ⁶⁵ CePIA, Departamento de Astronomía, Universidad de Concepción, Concepción, Chile

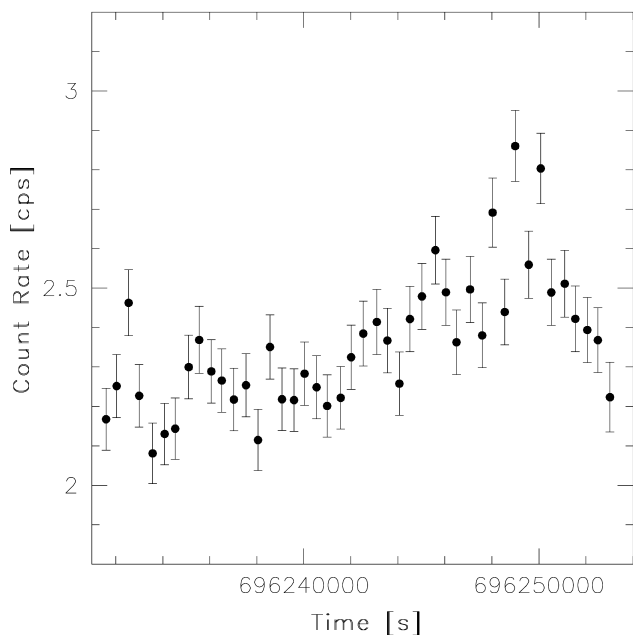


Fig. A.1. *XMM-Newton* EPIC pn light curve over 0.3–10 keV with 500 s bins of QSO B1420+326.

Appendix A:

Appendix A.1: *XMM-Newton* and *Swift-XRT* short-term variations

We have investigated short-term variability of the source in UV and X-rays by analyzing *Swift* and *XMM-Newton* data.

Correcting for instrumental artifacts and pile-up, no significant ($> 3\text{-}\sigma$) increase of count rate has been observed in the background-subtracted consecutive XRT observation segments.

We search also for significant ($> 3\text{-}\sigma$) changes of magnitude between two consecutive UVOT exposures collected with the same filter at the same epoch. This results in two events observed in *w1* filter on 2020 January 19 (MJD=58867) and 31 (MJD=58879), with a change of 0.16 mag in 27.6 ks and 0.41 mag in 34.4 ks, respectively.

Moreover, we produce a light curve of the *XMM-Newton* pn count rate with bin of 500 s (Fig. A.1). The light curve shows only moderate variability, with the count rate varying between 2.08 and 2.86 cps. The fractional variability (see Vaughan et al. 2003 for details) is 0.064 ± 0.005 . A larger variability has been observed in the second part of the observation, in particular an increase of $\sim 15\%$ of the count rate at the time of the highest peak.

Appendix A.2: *Swift-XRT* spectral fits

In Table A.1 we report the results of analysis of all *Swift-XRT* observations, including both historical observations and the ones performed during the high state of the source shown in detail in Fig. 1.

Appendix A.3: Long-term behaviour

In Fig. A.2 we report the monitoring observations of QSO B1420+326 in order to put the flaring state of January-February 2020 in the context of the long-term behaviour of the source. It

is clear that the flaring period has been unique in the *Fermi-LAT* dataset of this source. Similarly, the radio flux during the flare is also unique compared to previous measurements. On the other hand there is a prior report of a similar magnitude optical flare on 2016 March 11 (MJD=57458.5) in the ASAS-SN monitoring data (Stanek et al. 2017), however without a HE counterpart. Past X-ray data are unfortunately too sparse (and biased by Target of Opportunity observations) to judge about the typical behaviour of the source.

Date (UT)	MJD	Net exposure time (s)	Photon index (Γ_X)	Flux _{0.3–10keV} (10^{-12} erg cm $^{-2}$ s $^{-1}$)
2018-02-22	58171.915197	2872	1.49 ± 0.22	1.99 ± 0.37
2018-12-12	58464.132329	1818	1.51 ± 0.25	2.76 ± 0.54
2018-12-14	58466.253218	2110	1.37 ± 0.18	4.15 ± 0.65
2018-12-16	58468.386537	1943	1.50 ± 0.21	3.22 ± 0.54
2019-06-25	58659.880024	1975	1.89 ± 0.21	3.18 ± 0.45
2019-06-27/29	58663	2008	1.25 ± 0.24	3.07 ± 0.64
2019-07-12	58676.328225	1593	2.33 ± 0.15	7.11 ± 0.69
2019-07-17	58681.609499	1983	2.17 ± 0.15	4.83 ± 0.48
2019-07-22	58686.722614	1885	1.45 ± 0.22	2.98 ± 0.55
2019-12-13	58830.935420	2023	1.44 ± 0.13	7.85 ± 0.87
2020-01-02	58850.318109	2495	1.33 ± 0.17	5.47 ± 0.75
2020-01-05	58853.943061	1666	1.38 ± 0.27	4.09 ± 0.87
2020-01-08	58856.665569	1880	1.69 ± 0.20	3.73 ± 0.55
2020-01-11	58859.830600	1983	1.81 ± 0.17	5.54 ± 0.70
2020-01-19	58867.533771	1626	1.87 ± 0.15	5.88 ± 0.65
2020-01-21	58870.011577	1546	1.94 ± 0.16	6.00 ± 0.65
2020-01-24	58872.175468	1783	1.84 ± 0.14	6.57 ± 0.65
2020-01-25	58873.171868	1798	2.10 ± 0.14	7.12 ± 0.69
2020-01-27	58875.267506	1806	1.73 ± 0.19	4.42 ± 0.61
2020-01-28	58876.193806	2035	1.47 ± 0.18	4.80 ± 0.67
2020-01-31	58879.685875	1231	1.68 ± 0.19	5.88 ± 0.83
2020-02-01	58880.114444	1681	1.58 ± 0.16	5.87 ± 0.77
2020-02-05	58884.201846	2025	1.49 ± 0.15	6.30 ± 0.75
2020-02-10	58889.473095	2417	1.57 ± 0.18	3.50 ± 0.48

Table A.1. Log and fitting results of *Swift*-XRT observations of B2 1420+32 using a PL model. Fluxes are corrected for the Galactic absorption.

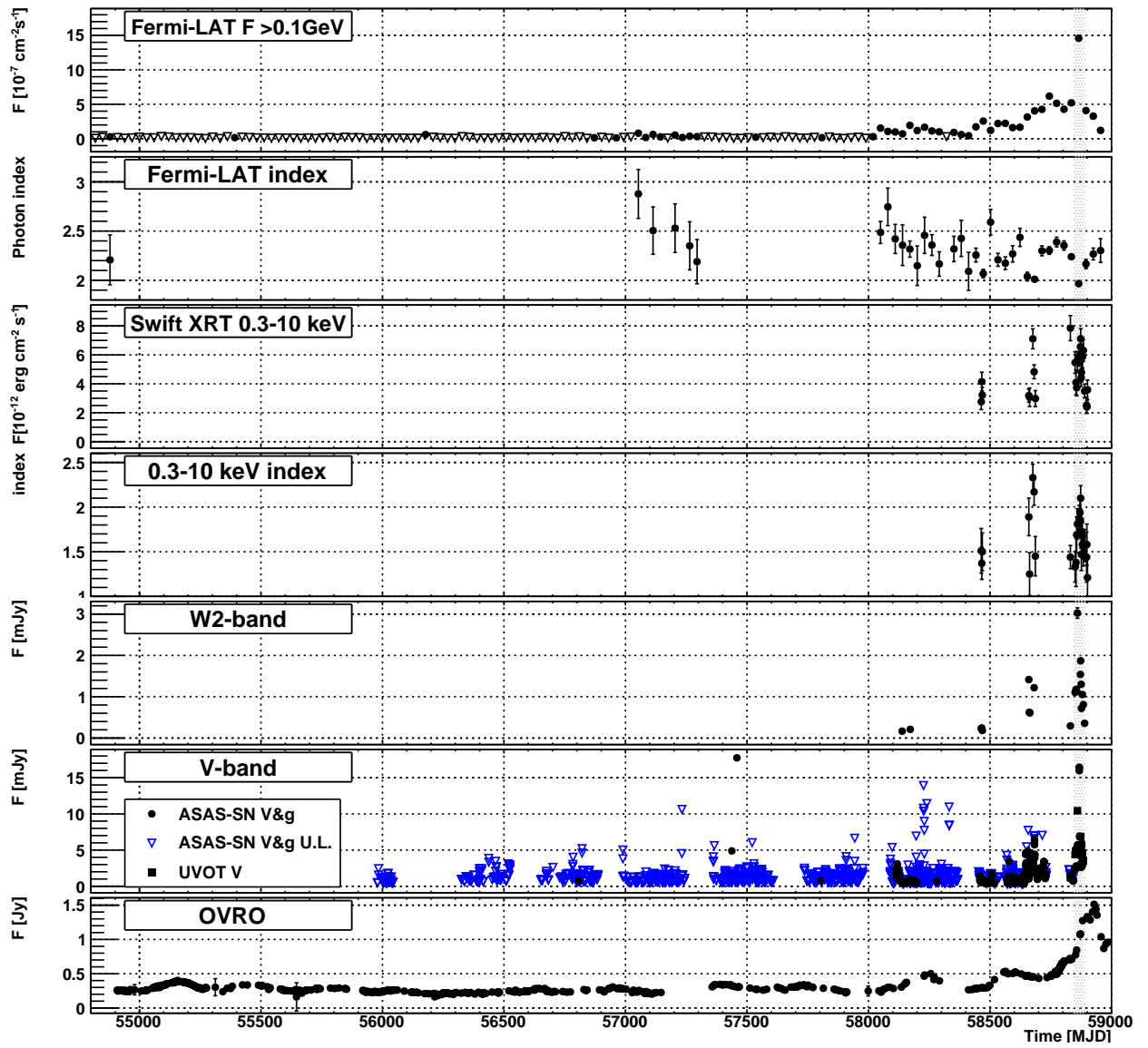


Fig. A.2. Long-term MWL light curve of QSO B1420+326 (see titles and legends of individual panels). The gray-shaded region shows the flaring period in the beginning of 2020.